A low Mach number diffuse-interface model for multicomponent two-phase flows with phase change

Journal of Computational Physics 523 (2025) 113683

Contents lists available at ScienceDirect

Journal of Computational Physics

journal homepage: www.elsevier.com/locate/jcp

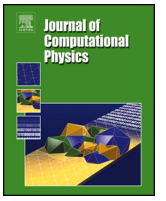

A low Mach number diffuse-interface model for multicomponent two-phase flows with phase change

Salar Zamani Salimi [a,*], Aritra Mukherjee [a], Marica Pelanti [c], Luca Brandt [a,b]

[a] Department of Energy and Process Engineering, Norwegian University of Science and Technology (NTNU), Trondheim, Norway
[b] Department of Environment, Land and Infrastructure Engineering (DIATI), Politecnico di Torino, Torino, Italy
[c] IMSIA, UMR 9219 ENSTA-CNRS-EDF, ENSTA Paris - Institut Polytechnique de Paris, 91120 Palaiseau, France

ARTICLE INFO

Keywords:
Multicomponent two-phase flows
Low Mach number
Phase change
Phase field model

ABSTRACT

This study introduces a four-equation, two-phase diffuse interface model designed to simulate two-phase, low-Mach flows with phase change. The model is extended to multicomponent gas by incorporating an additional equation for the vapor mass fraction transport. The methodology accounts for interfacial mass transfer driven by differences in the chemical potentials of the phases. A distinctive feature of our model is its ability to discretely conserve the mass of each phase, total momentum, and enthalpy, while maintaining a steady interface thickness, which is critical for the numerical stability and accuracy of two-phase flow simulations. Furthermore, the model effectively handles high density and viscosity ratios, making it robust across a wide range of applications. In addition to the general model suited for weakly compressible components, we also present a reduced model for fully incompressible components. The numerical methods are verified against several established benchmarks for fully incompressible systems with mass transfer. The low-Mach formulation is validated against sharp-interface simulations of the same problem; the results of a three-dimensional simulation of a sedimenting droplet undergoing evaporation are also illustrated.

1. Introduction

Multiphase flows involving heat and mass transfer are essential to many natural and industrial systems. Examples include rain formation [1], breaking waves [2], spray atomization [3] and bubbly flows [4,5]. The simultaneous exchange of mass, momentum, and energy across the phases' interfaces adds complexity to their study. The thickness of these interfaces is typically much smaller than other relevant flow scales, making accurate modeling challenging. These flows are characterized by moving and deforming interfaces that can undergo topological changes over time. Some classical models in the literature often assume spherical symmetry [6,7], and this simplification is appropriate only under microgravity conditions, where deformation and buoyancy effects are minimal [3]. For more accurate analysis of phase changes and complex chemical phenomena like combustion [8], multidimensional models are necessary to account for droplet deformation and surface tension effects. Despite these challenges, numerical simulations have become indispensable, complementing experiments that often struggle to capture detailed flow information [9]. Over the last decades, various numerical techniques have been developed to address the sharp property gradients and substantial deformations of the interfaces. These simulations provide valuable insights, necessary to improve product designs and system efficiencies. However, the intricate

* Corresponding author.
E-mail address: salar.z.salimi@ntnu.no (S.Z. Salimi).

https://doi.org/10.1016/j.jcp.2024.113683
Received 19 August 2024; Received in revised form 5 December 2024; Accepted 14 December 2024

Available online 18 December 2024

physics of interfacial transport and thermodynamic considerations still pose significant numerical challenges, triggering continued advancements in simulation methodologies.

One of the most challenging aspects of numerical modeling in multiphase flows is the method used to describe the motion of the liquid-gas interface, taking as example evaporation, the object of many examples in this work. This is typically achieved using a marker function, which assigns different values to each fluid and helps identify the interface. Methods for describing the interface can be broadly categorized into *interface tracking* and *interface capturing* methods.

Interface tracking methods, such as front-tracking (FT) [10,11], use Lagrangian markers to describe the interface motion. This allows for high precision in computing interface properties like normal vector and curvature. Hence, the FT method has been adapted to study boiling films [12] and evaporating droplets [13]. However, FT methods are limited in the case of complex configurations due to poor conservation properties [14] and difficulties in achieving parallel scalability on modern high-performance computing (HPC) architectures [15].

Interface capturing methods, including the Volume-of-Fluid (VoF) [16], Level-Set (LS) [17,18], and Phase-Field (PF) [19,20] methods, implicitly represent interfaces and offer improved conservation properties, particularly in cases with significant thermophysical property mismatches between phases. Despite these advantages, the implicit representation of interfaces presents challenges, such as accurately computing mass and energy exchanges at the interface. The VoF and LS methods are known as sharp-interface approaches, where thermophysical properties exhibit a jump across the interface. In recent years, several works have focused on coupling phase change with VoF method [21–30] or the LS method [31–35].

In contrast, phase-field methods, also known as diffuse interface approaches, represent thermophysical properties as functions of the local phase indicator function. The PF methods can resolve interfaces without requiring dedicated boundary conditions, they are thermodynamically motivated and utilize a free energy framework, allowing the inclusion of different physical effects through suitable modifications of the free energy. When combined with the Navier-Stokes equations to model interface convection, the PF method has successfully addressed problems like contact-line motion [36,37] and immiscible two-phase flows without phase change [38,39]. In these simulations, the flow field is assumed as incompressible, i.e., $\vec{\nabla} \cdot \vec{u} = 0$, where $\vec{u}$ denotes the velocity vector. The phase-field method is also used in the simulations of phase change such as solidification [40–42], boiling [12,43,44] and evaporation [45], assuming incompressible phases.

Traditionally, phase-field methods have been based on either the Cahn-Hilliard or Allen-Cahn equations, both of which are important gradient flows of the Ginzburg-Landau-Wilson free energy functional. The Allen-Cahn equation, a second-order PDE, is straightforward to implement and is extensively used in materials science applications involving phase transitions. However, the non-conservative form of the Allen-Cahn equation results in an inherent lack of mass conservation, posing a significant limitation when modeling immiscible two-phase flows.

On the other hand, the Cahn-Hilliard equation is in a conservative form and conserves total mass. For this particular phase-field method, Jacqmin [38] demonstrates how surface tension force can be defined so that total energy (kinetic energy plus surface energy) is only dissipated, thereby eliminating spurious currents. Generally, most studies on the Cahn-Hilliard equation, including Jacqmin [38], have focused on unity or low density ratios. However, the practical application of the Cahn-Hilliard equation in more complex configurations is limited by three drawbacks: (i) The artificial dissipation of total energy is undesirable, especially for realistic applications such as turbulent two-phase flows; (ii) handling the fourth-order spatial derivative is cumbersome; and (iii), most importantly, the equilibrium solution can lead to unbounded values at pure phases, which is unacceptable for high density ratios [46]. Some efforts have been made to eliminate these unbounded values, such as clipping [47] or adding correction terms to the Cahn-Hilliard equation [48,49]. However, these artificial modifications result in a method that is no longer a gradient flow of an energy functional and does not adhere to discrete conservation laws.

Due to the inherent deficiencies of traditional phase-field methods, Sun & Beckermann [50] omitted the curvature-driven flow in the Allen-Cahn equation to derive a second-order PDE suitable for two-phase simulations. Subsequently, Chiu & Lin [51] reformulated this phase-field model into a conservative form. However, the authors could not guarantee the boundedness of the phase field and had to employ mass redistribution to manage overshoots and undershoots. Finally, Mirjalili et al. [52] proved that using the same central-difference discretization employed in the reinitialization step of the conservative level-set method (CLS) [53] and with a proper choice of free parameters one can assure the boundedness of phase field. More recently, Jain et al. [54] proposed a conservative diffuse interface (CDI) method for simulating compressible two-phase flows, along with a boundedness proof that incorporates additional constraints on the free parameters specific to compressible flows. Building on these methods, this work adopts the methodology of [52] & [54] to accurately capture the interface and minimize diffusion in regions with strong variations in physical properties.

Furthermore, many engineering flows exhibit compressibility effects even when their velocities are relatively lower than the speed of sound, known as low-Mach flows. These flows possess characteristics of both fully compressible regimes (where pressure-density coupling dominates) and fully incompressible regimes (where pressure-velocity coupling dominates), making their numerical simulation challenging [55]. Common examples include cavitation, evaporation, and boiling. Although the phase transitions in these processes differ, they are all governed by the same physical mechanism: the equilibrium of the local Gibbs free energy between the two phases. While the liquid phase in these processes can be considered approximately incompressible, the significant heat and mass transfer rates induce compressibility in the gas phase, which cannot be ignored.

Compressible two-phase flows have been extensively studied over the past few decades, primarily using diffuse-interface methods. Despite the drawback of adopting an interface thickness much larger than the physical thickness, typically nanometers, these methods offer significant advantages for multiphase compressible flows. Firstly, they maintain thermodynamic consistency throughout the domain, including the interface where phase properties are averaged. Additionally, the diffuse interface allows for the numerical res-

Table 1
Summary of the differences between 4-, 5-, 6-, and 7-equation models, highlighting the number of mass, momentum, energy, and volume fraction equations in each.

Model	No. Mass Equations	No. Momentum Equations	No. Energy Equations	No. Volume Fraction Equations	Notation (M-Mo-E-V)
4-Equation	2	1	1	0	2-1-1-0
5-Equation	2	1	1	1	2-1-1-1
6-Equation	2	1	2	1	2-1-2-1
7-Equation	2	2	2	1	2-2-2-1

olution of property gradients, improving overall accuracy and stability. Furthermore, the natural dynamic creation and disappearance of interfaces, crucial for boiling and evaporation simulations, can be naturally captured by a PF method [56].

The diffuse-interface models for simulating compressible two-phase flows include models of different complexity. The seven-equation model of Baer–Nunziato [57,58] is the most general model, and it is able to account for full non-equilibrium (kinetic and thermodynamic) at interfaces between the phases. The model system is composed of a volume fraction equation for one phase and equations for the partial densities, momenta and total energies of the two phases (the classification of this model can be succinctly represented as 2-2-2-1; see Table 1 for details). Momentum, volume, heat and mass transfer processes driving the two-phase flow to kinetic, mechanical, thermal, and chemical equilibrium, respectively, can be taken into account by suitable relaxation source terms (relaxation of velocity, pressure, temperature, chemical potential, respectively). From the seven-equation model with relaxation terms a hierarchy of relaxed multiphase models can be derived by assuming instantaneous equilibria [59,60]. The six-equation model (2-1-2-1) [61–63] assumes kinetic equilibrium and it is typically combined with a stiff pressure relaxation procedure to model flows in mechanical equilibrium. The five-equation model (2-1-1-1) [64–68,54] assumes both kinetic and mechanical equilibrium, and consists of two mass balance equations for each phase, the volume fraction transport equation, and the equations for the mixture momentum and total energy. The four-equation model (2-1-1-0) [69–75] is obtained from the seven-equation model by assuming instantaneous kinetic, mechanical and thermal equilibrium between the two phases. The model retains the description of chemical non-equilibrium, hence the ability to account for mass transfer (and potentially other chemical processes). The four-equation (2-1-1-0) model in its conservative formulation is composed of the equations for the partial densities of the two phases, and the momentum and total energy equations for the mixture.

Relatively few studies have focused on weakly compressible multiphase flows. Notable among them are those based on the Baer–Nunziato model [76,77], based on the six-equation model [78], and various sharp interface methods [79–82]. These limited investigations have yielded encouraging outcomes in terms of numerical efficiency and overall performance across several test scenarios, including bubble oscillations and oscillating water columns.

As regards numerical models for phase change, recent advancements have seen researchers successfully couple phase transition with sharp-interface methods for the simulation of phase-changing (weakly-compressible) two-phase flows [83,82]. Although sharp-interface methods provide a more precise representation of interface shapes compared to diffuse-interface methods, they come with higher computational costs. These costs primarily arise due to function evaluation at the interface, causing challenges with load-balancing and scalability in parallel computing environments. In the case of compressible flows, diffuse-interface methods offer advantages because these flows inherently conserve the mass and not the volume of each phase, making the complex interface reconstruction and geometric advection processes in sharp-interface methods less beneficial. Additionally, sharp-interface methods require a semi-Lagrangian geometric method for advection to ensure mass conservation, which should make mass flux consistent with the volume flux calculated from the reconstructed interface. In contrast, diffuse-interface methods can simply use a mass balance equation to ensure mass conservation in each phase. Due to these factors, this study opts for a diffuse-interface approach. For an in-depth comparison of the two methods, we refer to [84].

In this paper, we present a novel diffuse-interface low Mach-number multicomponent two-phase flow model (2-1-1-0) capable of simulating weakly compressible flows with liquid-vapor transition. The model describes a two-phase flow composed of a liquid phase and a gaseous component consisting of the vaporized liquid species and an inert gas. The model is obtained by considering the low Mach number limit of an augmented four-equation two-phase flow model in our previous work [85], and by extending the resulting equations to the multicomponent case, which requires an additional equation for the vapor mass fraction. Although we derive a general model suited for weakly compressible components, in this work we then consider the limit of incompressible liquid, retaining the compressibility of the gaseous component. The proposed model accounts for interfacial mass transfer, which is driven by the difference of the chemical potentials of the phases. Our model offers several key features:

- It discretely conserves the mass of each phase, total momentum, and enthalpy.
- It ensures a steady interface thickness throughout the simulation using re-sharpening terms.
- It maintains the boundedness of the volume-fraction field, a critical requirement for simulating two-phase flows.
- It can handle complex equations of state and can handle high density and viscosity ratio.

The paper is structured as follows: Section 2 illustrates the mathematical derivation of the novel low-Mach number augmented four-equation two-phase flow model with mass transfer. The model is then extended to the multicomponent case for which we detail the formulation of the mass transfer term driven by the difference of the phasic chemical potentials. This section also discusses a simplified approach for fully incompressible components. Section 3 describes the numerical methods employed. Section 4 presents the verification of the method against established benchmarks for fully incompressible systems with mass transfer, validates the

low-Mach formulation against sharp-interface simulation results, and demonstrates a three-dimensional simulation of a fully-coupled system. The paper concludes in Section 5 with a summary of the main findings.

2. Mathematical formulation

2.1. Parent two-phase compressible flow model

The parent model of our formulation is a four-equation model that describes compressible two-phase flows in kinetic, mechanical and thermal equilibrium [72–74,86,75]. This model is obtained from the seven-equation non-equilibrium two-phase flow model of Baer–Nunziato [57,58] in the limit of instantaneous pressure, velocity and temperature relaxation (see derivation from the Baer–Nunziato model in [75]). We will denote with α_k, ρ_k, $\mathcal{E}_k$ the volume fraction, density, internal energy per unit volume of phase k, $k = 1, 2$. Moreover we will denote with p, T and $\vec{u}$ the pressure, temperature and velocity field. The mixture density is $\rho = \sum_{k=1}^{2} \alpha_k \rho_k$, the mixture internal energy $\mathcal{E} = \sum_{k=1}^{2} \alpha_k \mathcal{E}_k$, and the mixture total energy $E = \sum_{k=1}^{2} \alpha_k E_k$, $E_k = \mathcal{E}_k + \rho_k \frac{|\vec{u}|^2}{2}$. We account for mass transfer, viscous stresses, surface tension, heat conduction, and gravity. In conservative form the model reads:

$$\partial_t(\alpha_1\rho_1) + \vec{\nabla}\cdot(\alpha_1\rho_1\vec{u}) = \mathcal{M}, \tag{1a}$$

$$\partial_t(\alpha_2\rho_2) + \vec{\nabla}\cdot(\alpha_2\rho_2\vec{u}) = -\mathcal{M}, \tag{1b}$$

$$\partial_t(\rho\vec{u}) + \vec{\nabla}\cdot(\rho\vec{u}\otimes\vec{u} + p\mathbb{I}) = \vec{\nabla}\cdot\vec{\tau} + \vec{\Sigma} + \rho\vec{\mathfrak{g}}, \tag{1c}$$

$$\partial_t E + \vec{\nabla}\cdot((E+p)\vec{u}) = \vec{\nabla}\cdot(\vec{\tau}\cdot\vec{u}) - \vec{\nabla}\cdot\vec{q} + \vec{\Sigma}\cdot\vec{u} + \rho\vec{\mathfrak{g}}\cdot\vec{u}. \tag{1d}$$

Above $\vec{\tau} = \alpha_1\vec{\tau}_1 + \alpha_2\vec{\tau}_2$ is the viscous stress tensor, with $\vec{\tau}_k$ denoting the viscous stress for the phase k, $k = 1, 2$. We assume the Newtonian constitutive relation $\vec{\tau} = \mu(\vec{\nabla}\vec{u} + \vec{\nabla}\vec{u}^{\mathrm{T}}) - \frac{2}{3}\mu(\vec{\nabla}\cdot\vec{u})\vec{I}$, $\mu = \alpha_1\mu_1 + \alpha_2\mu_2$, where μ_k is the dynamic viscosity of phase k. Moreover, $\vec{\mathfrak{g}}$ is the specific gravity force and $\vec{\Sigma} = \sigma\kappa\vec{\nabla}\alpha_1$ is the surface tension, where σ is the surface tension coefficient and $\kappa = -\vec{\nabla}\cdot\left(\frac{\vec{\nabla}\alpha_1}{|\vec{\nabla}\alpha_1|}\right)$ represents the local curvature. Heat conduction is modeled by the heat flux $\vec{q} = -\lambda_c\vec{\nabla}T$ (using Fourier law), where the mixture thermal conductivity is expressed as $\lambda_c = \alpha_1\lambda_{c1} + \alpha_2\lambda_{c2}$, with λ_{ck} the thermal conductivity of phase k. The source term $\mathcal{M}$ is the mass transfer term, whose expression will be detailed later (Section 2.4 and Appendix C for the case of boiling). The model is closed with an equation of state for each phase, e.g. by relations $p_k(\mathcal{E}_k, \rho_k)$ and $T_k(\mathcal{E}_k, \rho_k)$. Given these laws for each phase, the mixture equation of state is determined by the mechanical and thermal equilibrium conditions $p_1 = p_2 = p$, $T_1 = T_2 = T$, together with the mixture energy relation $\mathcal{E} = \alpha_1\mathcal{E}_1 + \alpha_2\mathcal{E}_2$. Within this formulation, the speed of sound c is defined by (see for instance [87])

$$\frac{1}{c^2} = \rho\left(\frac{\alpha_1}{\rho_1 c_1^2} + \frac{\alpha_2}{\rho_2 c_2^2}\right) + \frac{\rho T C_{p1} C_{p2}}{C_{p1} + C_{p2}}\left(\frac{\Gamma_2}{\rho_2 c_2^2} - \frac{\Gamma_1}{\rho_1 c_1^2}\right)^2, \tag{2}$$

where c_k is the speed of sound of phase k, which can be expressed as

$$c_k = \sqrt{\Gamma_k h_k + \chi_k}, \qquad \Gamma_k = \left(\frac{\partial p_k}{\partial \mathcal{E}_k}\right)_{\rho_k}, \qquad \chi_k = \left(\frac{\partial p_k}{\partial \rho_k}\right)_{\mathcal{E}_k}, \tag{3}$$

where $h_k = \frac{\mathcal{E}_k + p_k}{\rho_k}$ is the phasic specific enthalpy and Γ_k is the Grüneisen coefficient. In eq. (2), we have also defined the extensive heat capacities $C_{pk} = \alpha_k\rho_k\kappa_{pk}$, where $\kappa_{pk} = \frac{\partial h_k}{\partial T_k}\Big|_{p_k} = T_k\frac{\partial s_k}{\partial T_k}\Big|_{p_k}$ is the specific heat capacity at constant pressure. Let us also write for later use the equation for the pressure:

$$\partial_t p + \vec{u}\cdot\vec{\nabla}p + \rho c^2\vec{\nabla}\cdot\vec{u} = S_p\,\mathcal{M} + S_p^e(\vec{\nabla}\vec{u} : \vec{\tau} + \vec{\nabla}\cdot(\lambda_c\vec{\nabla}T)), \tag{4}$$

where c is the speed of sound defined by (2), and

$$S_p = \frac{1}{D_T}\left[\left(\frac{\chi_1}{\Gamma_1} - \frac{\chi_2}{\Gamma_2}\right)(\alpha_1\phi_1\rho_2 + \alpha_2\phi_2\rho_1) + \left(\frac{\rho_2 c_2^2}{\Gamma_2} - \frac{\rho_1 c_1^2}{\Gamma_1}\right)(\alpha_1\phi_1 + \alpha_2\phi_2)\right], \tag{5}$$

$$S_p^e = \frac{1}{D_T}(\alpha_1\phi_1\rho_2 + \alpha_2\phi_2\rho_1), \tag{6}$$

with

$$D_T = \alpha_1\alpha_2\left(\frac{\rho_1 c_1^2}{\Gamma_1} - \frac{\rho_2 c_2^2}{\Gamma_2}\right)(\phi_1\zeta_2 - \phi_2\zeta_1) + \left(\frac{\alpha_1}{\Gamma_1} + \frac{\alpha_2}{\Gamma_2}\right)(\alpha_1\phi_1\rho_2 + \alpha_2\phi_2\rho_1). \tag{7}$$

In the expressions above, ϕ_k and ζ_k are defined as

$$\phi_k = \left(\frac{\partial\rho_k}{\partial T_k}\right)_{p_k} = -\rho_k\beta_k \quad \text{and} \quad \zeta_k = \left(\frac{\partial\rho_k}{\partial p_k}\right)_{T_k} = \rho_k K_{Tk}, \tag{8}$$

Table 2
Nomenclature of variables and parameters.

ρ_k = phasic density
α_k = volume fraction of phase k ($\alpha_1 + \alpha_2 = 1$)
$\alpha_k \rho_k$ = partial density of phase k
$\vec{u}$ = velocity vector
ε_k = phasic specific internal energy
$\mathcal{E}_k = \rho_k \varepsilon_k$ = phasic internal energy per unit volume
$E_k = \mathcal{E}_k + \rho_k \frac{\lvert\vec{u}\rvert^2}{2}$ = phasic total energy per unit volume
p_k = phasic pressure
p = mixture equilibrium pressure
$\rho = \alpha_1 \rho_1 + \alpha_2 \rho_2$ = mixture density
$Y_k = \frac{\alpha_k \rho_k}{\rho}$ = mass fraction of phase k ($Y_1 + Y_2 = 1$)
$\varepsilon = Y_1 \varepsilon_1 + Y_2 \varepsilon_2$ = mixture specific internal energy
$\mathcal{E} = \rho\varepsilon = \alpha_1 \mathcal{E}_1 + \alpha_2 \mathcal{E}_2$ = mixture internal energy per unit volume
$E = \mathcal{E} + \frac{1}{2}\rho\lvert\vec{u}\rvert^2 = \alpha_1 E_1 + \alpha_2 E_2$ = mixture total energy per unit volume
$h_k = \frac{\mathcal{E}_k + p_k}{\rho_k}$ = phasic specific enthalpy
$h = Y_1 h_1 + Y_2 h_2$ = mixture specific enthalpy
$c_k = \sqrt{\left(\frac{\partial p_k}{\partial \rho_k}\right)_{s_k}}$ = sound speed of phase k
T_k = phasic temperature
T = mixture equilibrium temperature
s_k = phasic entropy
$s = Y_1 s_1 + Y_2 s_2$ = mixture entropy
μ_k^p = phasic chemical potential
g_k = phasic Gibbs free energy
$\Gamma_k = \left(\frac{\partial p_k}{\partial \mathcal{E}_k}\right)_{\rho_k}$ = Grüneisen coefficient of phase k
$\chi_k = \left(\frac{\partial p_k}{\partial \rho_k}\right)_{\mathcal{E}_k}$
$\phi_k = \left(\frac{\partial p_k}{\partial T_k}\right)_{p_k} = -\rho_k \beta_k$, β_k = phasic coefficient of thermal expansion
$\zeta_k = \left(\frac{\partial \rho_k}{\partial p_k}\right)_{T_k} = \rho_k K_{Tk}$, K_{Tk} = phasic isothermal compressibility
$K_{Sk} = \frac{1}{\rho_k c_k^2}$ = phasic isentropic compressibility
$\kappa_{pk} = T_k \left(\frac{\partial s_k}{\partial T_k}\right)_{p_k} = \left(\frac{\partial h_k}{\partial T_k}\right)_{p_k}$ = specific heat capacity at constant pressure
$\kappa_{\upsilon k} = T_k \left(\frac{\partial s_k}{\partial T_k}\right)_{\rho_k} = \left(\frac{\partial \varepsilon_k}{\partial T_k}\right)_{\rho_k}$ = specific heat capacity at constant volume
$C_{pk} = \alpha_k \rho_k \kappa_{pk}$ = phasic extensive heat capacity at constant pressure
λ_c = mixture thermal conductivity
$\vec{\tau}$ = mixture viscous stress tensor
$\vec{\Sigma}$ = surface tension
$\vec{\mathfrak{g}}$ = specific gravity force
ξ = vapor mass fraction in the gas phase
μ = dynamic viscosity of the mixture

where β_k denotes the coefficient of thermal expansion and K_{Tk} the isothermal compressibility. For completeness, we also report here some useful thermodynamic relations:

$$\beta_k = \frac{\Gamma_k \kappa_{pk}}{c_k^2}, \quad K_{Tk} = K_{Sk} + \frac{\beta_k^2 T_k}{\rho_k \kappa_{pk}}, \quad K_{Sk} = \frac{1}{\rho_k c_k^2}. \tag{9}$$

Let us note that the quantity $\mathcal{S}_p^e$ in (6) reduces to Γ in single-phase flows.

We finally write the equation for (ρh) where h is the specific mixture enthalpy, $h = \frac{\mathcal{E}+p}{\rho} = Y_1 h_1 + Y_2 h_2$, with $Y_1 = \frac{\alpha_1 \rho_1}{\rho}$ the mass fraction:

$$\partial_t(\rho h) + \vec{\nabla} \cdot (\rho h \vec{u}) + \rho c^2 \vec{\nabla} \cdot \vec{u} = \mathcal{S}_p \mathcal{M} + (1 + \mathcal{S}_p^e)(\vec{\nabla}\vec{u} : \vec{\tau} + \vec{\nabla} \cdot (\lambda_c \vec{\nabla} T)). \tag{10}$$

As shown later, in the low Mach number limit the equation for the enthalpy per unit volume (ρh) has a convenient conservative form. The nomenclature used is summarized in Table 2.

2.2. Low Mach number two-phase flow model

We derive in this section a low-Mach number formulation from the two-phase flow model in equation (1). Theoretically, the asymptotic behavior as the Mach number vanishes of solutions of the compressible Euler equations, the compressible Navier–Stokes equations, or of more complex phenomena such as combustion, has been studied by many authors, e.g. [88–93]. A classical approach to tackle the low-Mach number limit of the equations consists in writing the system in non-dimensional form and performing an asymptotic expansion of the non-dimensional variables in powers of a reference Mach number M_r. We apply here the same approach to the two-phase model under investigation.

2.2.1. Non-dimensional equations

We wish to write the non-dimensional equations for the partial densities $\alpha_k\rho_k$, the momentum $\rho\vec{u}$, the pressure p, and the mixture enthalpy per unit volume ρh. We indicate non-dimensional variables with an accent $\acute{(\cdot)}$, and denote with subscript r the reference quantities. We introduce the non-dimensionalized variables

$$\acute{\rho} = \frac{\rho}{\rho_r}, \quad \acute{\rho}_k = \frac{\rho_k}{\rho_r}, \quad \acute{\alpha}_k = \alpha_k, \quad \acute{Y}_k = Y_k, \qquad \vec{\acute{u}} = \frac{\vec{u}}{u_r}, \quad \vec{\acute{x}} = \frac{\vec{x}}{l_r}, \quad \acute{t} = \frac{t}{t_r}, \quad t_r = \frac{l_r}{u_r}, \tag{11}$$

$$\acute{p} = \frac{p}{p_r}, \quad \acute{\mathcal{E}} = \frac{\mathcal{E}}{p_r}, \quad \acute{\mathcal{E}}_k = \frac{\mathcal{E}_k}{p_r}, \quad \acute{h} = \frac{h}{p_r/\rho_r}, \quad \acute{h}_k = \frac{h_k}{p_r/\rho_r}, \tag{12}$$

where l_r is a length scale. Moreover we define the reference speed of sound c_r and the Mach number M_r as:

$$c_r^2 = \frac{p_r}{\rho_r}, \quad M_r = \frac{u_r}{c_r}. \tag{13}$$

We also define:

$$\acute{c} = \frac{c}{c_r}, \quad \acute{T} = \frac{T}{T_r}, \quad T_r = \frac{p_r}{\rho_r\kappa_{pr}} = \frac{c_r^2}{\kappa_{pr}}, \quad \vec{\vec{\acute{\tau}}} = \frac{\vec{\vec{\tau}}}{\vec{\vec{\tau}}_r}, \quad \vec{\vec{\tau}}_r = \frac{\mu_r u_r}{l_r}, \quad \acute{\lambda}_c = \frac{\lambda_c}{\lambda_{cr}}, \tag{14}$$

where κ_{pr}, μ_r and λ_{cr} are reference values for the specific heat, the dynamic viscosity and the thermal conductivity, respectively. We then introduce the Reynolds number Re the Froude number Fr, the Weber number We, and the Prandtl number Pr:

$$\mathrm{Re} = \frac{\rho_r u_r l_r}{\mu_r}, \quad \mathrm{Fr} = \frac{u_r}{\sqrt{\mathfrak{g}_r l_r}}, \quad \mathrm{We} = \frac{\rho_r u_r^2 l_r}{\sigma_r}, \quad \mathrm{Pr} = \frac{\kappa_{pr}\mu_r}{\lambda_{cr}}, \tag{15}$$

with $\mathfrak{g}_r$ and σ_r denoting a reference gravity field and a reference surface tension coefficient. We denote the time scale for mass transfer with t_r^M, and express the non-dimensional mass transfer term as:

$$\acute{\mathcal{M}} = \frac{\mathcal{M}}{\mathcal{M}_r}, \quad \mathcal{M}_r = \frac{\rho_r}{t_r^M} = \frac{\Phi\rho_r}{t_r}, \quad \Phi = \frac{t_r}{t_r^M}. \tag{16}$$

Moreover, we define:

$$\acute{\mathcal{S}}_p = \frac{\mathcal{S}_p}{\mathcal{S}_{pr}}, \quad \mathcal{S}_{pr} = c_r^2 = \frac{p_r}{\rho_r}, \tag{17}$$

and note that the quantity $\mathcal{S}_p^e$ defined in (6) is already non-dimensional, $\acute{\mathcal{S}}_p^e = \mathcal{S}_p^e$. Finally, we obtain the following non-dimensional equations for the partial densities, the mixture momentum, the pressure, and the enthalpy:

$$\partial_{\acute{t}}(\alpha_1\acute{\rho}_1) + \vec{\acute{\nabla}}\cdot(\alpha_1\acute{\rho}_1\vec{\acute{u}}) = \Phi\acute{\mathcal{M}}, \tag{18a}$$

$$\partial_{\acute{t}}(\alpha_2\acute{\rho}_2) + \vec{\acute{\nabla}}\cdot(\alpha_2\acute{\rho}_2\vec{\acute{u}}) = -\Phi\acute{\mathcal{M}}, \tag{18b}$$

$$\partial_{\acute{t}}(\acute{\rho}\vec{\acute{u}}) + \vec{\acute{\nabla}}\cdot(\acute{\rho}\vec{\acute{u}}\otimes\vec{\acute{u}}) + \frac{\vec{\acute{\nabla}}\acute{p}}{M_r^2} = \frac{1}{\mathrm{Re}}\vec{\acute{\nabla}}\cdot\vec{\vec{\acute{\tau}}} - \frac{\acute{\sigma}}{\mathrm{We}}\vec{\acute{\nabla}}\cdot\left(\frac{\vec{\acute{\nabla}}\alpha_1}{|\vec{\acute{\nabla}}\alpha_1|}\right)\vec{\acute{\nabla}}\alpha_1 + \frac{1}{\mathrm{Fr}^2}\acute{\rho}\vec{\mathfrak{g}}, \tag{18c}$$

$$\partial_{\acute{t}}\acute{p} + \vec{\acute{u}}\cdot\vec{\acute{\nabla}}\acute{p} + \acute{\rho}\acute{c}^2\vec{\acute{\nabla}}\cdot\vec{\acute{u}} = \acute{\mathcal{S}}_p\Phi\acute{\mathcal{M}} + \frac{\mathcal{S}_p^e M_r^2}{\mathrm{Re}}\vec{\acute{\nabla}}\vec{\acute{u}} : \vec{\vec{\acute{\tau}}} + \frac{\mathcal{S}_p^e}{\mathrm{Re}\,\mathrm{Pr}}\vec{\acute{\nabla}}\cdot(\acute{\lambda}_c\vec{\acute{\nabla}}\acute{T}), \tag{18d}$$

$$\partial_{\acute{t}}(\acute{\rho}\acute{h}) + \vec{\acute{\nabla}}\cdot(\acute{\rho}\acute{h}\vec{\acute{u}}) + \acute{\rho}\acute{c}^2\vec{\acute{\nabla}}\cdot\vec{\acute{u}} = \acute{\mathcal{S}}_p\Phi\acute{\mathcal{M}} + (1+\mathcal{S}_p^e)\left(\frac{M_r^2}{\mathrm{Re}}\vec{\acute{\nabla}}\vec{\acute{u}} : \vec{\vec{\acute{\tau}}} + \frac{1}{\mathrm{Re}\,\mathrm{Pr}}\vec{\acute{\nabla}}\cdot(\acute{\lambda}_c\vec{\acute{\nabla}}\acute{T})\right). \tag{18e}$$

2.2.2. Low Mach number equations

Now we assume asymptotic expansions of any variable $\varphi(\vec{x},t)$ of the form

$$\varphi(\vec{x},t) = \varphi(\vec{x},t)^{[0]} + \varphi^{[1]}(\vec{x},t)M_r + \varphi^{[2]}(\vec{x},t)M_r^2 + \dots \tag{19}$$

Introducing the asymptotic expansions in (18) and collecting terms with the same order in M_r, one obtains $\nabla \acute{p}^{[0]} = 0$ and $\nabla \acute{p}^{[1]} = 0$ at order M_r^{-2} and at order M_r^{-1}, respectively. This implies that the pressure is constant in space up to perturbations of order M_r^2. Therefore, we can write

$$\acute{p}(\vec{\acute{x}}, \acute{t}) = \acute{p}^{[0]}(\acute{t}) + \acute{p}^{[2]}(\vec{\acute{x}}, \acute{t}) M_r^2 + \dots , \tag{20}$$

with $\acute{p}^{[0]}(\acute{t}) = \acute{p}_0(\acute{t})$, where $\acute{p}_0$ is the non-dimensional background thermodynamic pressure, $\acute{p}_0(\acute{t}) = \frac{p_0(t)}{p_r}$. In the presence of open boundaries with a constant exterior pressure $\bar{p}_0$ we have $p_0 = \bar{p}_0 = \text{constant}$. At order M_r^0 we have a system of the form:

$$\partial_{\acute{t}}(\alpha_1 \acute{\rho}_1) + \vec{\acute{\nabla}} \cdot (\alpha_1 \acute{\rho}_1 \vec{\acute{u}}) = \Phi \acute{\mathcal{M}} , \tag{21a}$$

$$\partial_{\acute{t}}(\alpha_2 \acute{\rho}_2) + \vec{\acute{\nabla}} \cdot (\alpha_2 \acute{\rho}_2 \vec{\acute{u}}) = -\Phi \acute{\mathcal{M}} , \tag{21b}$$

$$\partial_{\acute{t}}(\acute{\rho}\vec{\acute{u}}) + \vec{\acute{\nabla}} \cdot (\acute{\rho}\vec{\acute{u}} \otimes \vec{\acute{u}}) + \vec{\acute{\nabla}}\acute{\tilde{p}} = \frac{1}{\mathrm{Re}} \vec{\acute{\nabla}} \cdot \vec{\vec{\acute{\tau}}} - \frac{\acute{\sigma}}{\mathrm{We}} \vec{\acute{\nabla}} \cdot \left(\frac{\vec{\acute{\nabla}}\alpha_1}{|\vec{\acute{\nabla}}\alpha_1|} \right) \vec{\acute{\nabla}}\alpha_1 + \frac{1}{\mathrm{Fr}^2} \acute{\rho}\vec{\mathfrak{g}} , \tag{21c}$$

$$\vec{\acute{\nabla}} \cdot \vec{\acute{u}} = \frac{\acute{\mathcal{S}}_p}{\acute{\rho}\acute{c}^2(Y_1, \acute{h}, \acute{p}_0)} \Phi \acute{\mathcal{M}} + \frac{\mathcal{S}_p^e}{Re\, Pr \acute{\rho}\acute{c}^2(Y_1, \acute{h}, \acute{p}_0)} \vec{\acute{\nabla}} \cdot (\acute{\lambda}_c \vec{\acute{\nabla}}\acute{T}) - \frac{1}{\acute{\rho}\acute{c}^2(Y_1, \acute{h}, \acute{p}_0)} \frac{d\acute{p}_0(\acute{t})}{d\acute{t}} , \tag{21d}$$

$$\partial_{\acute{t}}(\acute{\rho}\acute{h}) + \vec{\acute{\nabla}} \cdot (\acute{\rho}\acute{h}\vec{\acute{u}}) = \frac{1}{\mathrm{Re}\,\mathrm{Pr}} \vec{\acute{\nabla}} \cdot (\acute{\lambda}_c \vec{\acute{\nabla}}\acute{T}) + \frac{d\acute{p}_0(\acute{t})}{d\acute{t}} , \tag{21e}$$

where we have omitted the superscripts [0] for all the variables ρ, α_k, ρ_k, $\vec{u}$, h, and set $\acute{\tilde{p}} \equiv \acute{p}^{[2]}$. $\acute{\tilde{p}}$ represents the dimensionless perturbation of the dimensionless thermodynamic pressure $\acute{p}_0$, and it is a dynamic pressure with no thermodynamic meaning. The dimensional form of the pressure perturbation is $\tilde{p} = \rho_r u_r^2 \acute{\tilde{p}}$. Note that we can obtain an equation for $\frac{d\acute{p}_0(\acute{t})}{d\acute{t}}$ by integrating the equation (21d) for $\vec{\acute{\nabla}} \cdot \vec{\acute{u}}$ over the considered flow domain (see corresponding dimensional equation for $\frac{dp_0(t)}{dt}$ in (23)). Finally, the dimensional form of the system is:

$$\partial_t(\alpha_1 \rho_1) + \vec{\nabla} \cdot (\alpha_1 \rho_1 \vec{u}) = \mathcal{M} , \tag{22a}$$

$$\partial_t(\alpha_2 \rho_2) + \vec{\nabla} \cdot (\alpha_2 \rho_2 \vec{u}) = -\mathcal{M} , \tag{22b}$$

$$\partial_t(\rho\vec{u}) + \vec{\nabla} \cdot (\rho\vec{u} \otimes \vec{u}) + \vec{\nabla}\tilde{p} = \vec{\nabla} \cdot \vec{\vec{\tau}} + \vec{\Sigma} + \rho\vec{\mathfrak{g}} , \tag{22c}$$

$$\vec{\nabla} \cdot \vec{u} = \frac{\mathcal{S}_p}{\rho c^2(Y_1, h, p_0)} \mathcal{M} + \frac{\mathcal{S}_p^e}{\rho c^2(Y_1, h, p_0)} \vec{\nabla} \cdot (\lambda_c \vec{\nabla} T) - \frac{1}{\rho c^2(Y_1, h, p_0)} \frac{dp_0(t)}{dt} , \tag{22d}$$

$$\partial_t(\rho h) + \vec{\nabla} \cdot (\rho h \vec{u}) = \vec{\nabla} \cdot (\lambda_c \vec{\nabla} T) + \frac{dp_0(t)}{dt} . \tag{22e}$$

Let us note that the five-equation system (22) (or (21)) is over-determined since four equations (with the equations of state) would be enough to completely determine the solution, as in the parent four-equation model (1). Nonetheless, we adopt this augmented four-equation system for numerical purposes, namely to ensure mass conservation for both phases (as we proposed for the model in [85]), while we compute efficiently the temperature via an enthalpy equation. We observe that in choosing the set of equations to be solved numerically we would like to retain the phasic mass and momentum conservation laws, together with the equation for $\vec{\nabla} \cdot \vec{u}$. Moreover, we would like to retain an equation for a thermodynamic variable (e.g. internal energy, enthalpy, temperature) that would allow us to compute efficiently the temperature. Here we have chosen the equation for the enthalpy per unit volume ρh (as e.g. in [94]) since in the low Mach number limit this equation has a conservative form, at least when the term $dp_0(t)/dt = 0$ (problems where the background pressure p_0 is constant, such as in the case of open systems). Moreover, in the asymptotic limit of stationary conditions this enthalpy equation gives a conservation law expressing the balance of the enthalpy flux with the heat conduction flux. Let us note that in order to have a framework that could include models with one or more incompressible phases (constant ρ_k), such as the multicomponent models presented below in Section 2.3 and Section 2.5, an enthalpy equation (or energy or temperature equation) is strictly needed, since the temperature cannot be recovered from the mass equations in these cases. Indeed we see that the formula to compute T via the densities $\frac{1}{\rho} = \frac{Y_1}{\rho_1(p_0,T)} + \frac{Y_2}{\rho_2(p_0,T)}$ could be used for compressible components only. The adopted augmented four-equation system (22) allows us to guarantee numerically conservation for the mass of both phases, for the momentum, for the enthalpy per unit volume (when $dp_0(t)/dt = 0$), and to compute efficiently the temperature via $h = Y_1 h_1(p_0, T) + Y_2 h_2(p_0, T)$ or $\rho h = \alpha_1 \rho_1 h_1(p_0, T) + \alpha_2 \rho_2 h_2(p_0, T)$.

Finally let us remark that by integrating (22d) over a volume Ω we have:

$$\frac{dp_0(t)}{dt} = -\frac{1}{|\Omega|} \int_\Omega \rho c^2 \vec{\nabla} \cdot \vec{u}\, dV - \frac{1}{|\Omega|} \int_\Omega \mathcal{S}_p^e \vec{\nabla} \cdot \vec{q}\, dV + \frac{1}{|\Omega|} \int_\Omega \mathcal{S}_p \mathcal{M}\, dV , \tag{23}$$

which can be used to determine the evolution of the thermodynamic pressure in closed systems (recalling that $\vec{q} = -\lambda_c \vec{\nabla} T$). Note that the initial condition needs to satisfy eq. (22d) for compatibility. The model system above (22) can be used to describe flows composed in general of two weakly compressible fluids, each governed by an arbitrary equation of state (see also the model for boiling flows

in Appendix C). In the next section we will consider a simpler model where one phase is incompressible, aiming to applications with evaporation.

2.3. Multicomponent liquid-vapor-gas model with mass transfer

We use the low-Mach number model (22) derived above to describe flows with liquid-gas interfaces. The liquid phase (denoted as phase 1) here is assumed incompressible, while the gaseous phase (denoted as phase 2) is considered weakly compressible. For the liquid we have

$$\rho_1 = \text{constant}\,, \quad h_1 = \kappa_{p1} T + \eta_1\,, \tag{24}$$

where the specific enthalpy of formation η_1 is a constant. The specific heat capacity κ_{p1} is also assumed constant. The liquid species can undergo phase change, and we consider that the gaseous phase is composed of the vapor of the liquid species (denoted with subscript v) and a non-condensible gas, for instance air (denoted with subscript a). This gas mixture is modeled as a mixture of ideal gases obeying Dalton's law of partial pressures:

$$p = p_v + p_a\,. \tag{25}$$

In this model each gas component of the mixture is assumed to occupy the volume V_2 of the mixture, $V_v = V_a = V_2$. Noting that the densities are $\rho_v = \mathfrak{m}_v/V_v = \mathfrak{m}_v/V_2$, $\rho_a = \mathfrak{m}_a/V_a = \mathfrak{m}_a/V_2$, where $\mathfrak{m}$ denotes the mass, and since $\mathfrak{m}_2 = \mathfrak{m}_v + \mathfrak{m}_a$, we have:

$$\rho_2 = \rho_v + \rho_a\,. \tag{26}$$

The vapor mass fraction $\xi = \mathfrak{m}_v/\mathfrak{m}_2$ in the gaseous phase is thus given by

$$\xi = \frac{\rho_v}{\rho_2}\,. \tag{27}$$

The specific enthalpy and energy become

$$h_2 = \xi h_v + (1-\xi) h_a\,, \qquad \varepsilon_2 = \xi \varepsilon_v + (1-\xi)\varepsilon_a\,, \tag{28}$$

where $\varepsilon = \frac{\mathcal{E}}{\rho}$ and

$$\rho_2 h_2 = \rho_v h_v + \rho_a h_a\,, \qquad \mathcal{E}_2 = \mathcal{E}_v + \mathcal{E}_a\,. \tag{29}$$

We now define the equation of state for the ideal gas mixture:

$$p = \rho_2 \frac{\mathcal{R}}{M_2(\xi)} T\,, \quad h_2 = \kappa_{p2}(\xi) T\,, \tag{30}$$

where $\mathcal{R}$ denotes the universal gas constant, and

$$\frac{1}{M_2(\xi)} = \frac{\xi}{M_v} + \frac{1-\xi}{M_a}\,, \quad \kappa_{p2}(\xi) = \xi \kappa_{pv} + (1-\xi)\kappa_{pa}\,, \tag{31}$$

where M_v and M_a are the molar masses of the liquid-vapor species and of the non-condensible gas, respectively. The specific heat capacities κ_{pv}, κ_{vv}, κ_{pa}, κ_{va} of the vapor and inert gas are constant. Note that we also have

$$\kappa_{v2}(\xi) = \xi \kappa_{vv} + (1-\xi)\kappa_{va}\,, \quad \gamma_2(\xi) = \frac{\kappa_{p2}(\xi)}{\kappa_{v2}(\xi)} = \frac{\xi \kappa_{pv} + (1-\xi)\kappa_{pa}}{\xi \kappa_{vv} + (1-\xi)\kappa_{va}}\,. \tag{32}$$

The gas mixture speed of sound is $c_2(\xi) = \sqrt{\frac{\gamma_2(\xi) p}{\rho_2(\xi)}} = \sqrt{\gamma_2(\xi) R_2(\xi) T}$, and the Grüneisen coefficient $\Gamma_2(\xi) = \gamma_2(\xi) - 1$. We also recall the relation for ideal gases $R_2 = \kappa_{p2}\frac{\gamma_2 - 1}{\gamma_2}$. Note that in the low-Mach number model $p = p_0(t)$ (thermodynamic pressure).

Considering the liquid incompressible, the mass equations for the liquid and gas phases in the model (22) take the form:

$$\partial_t \alpha_1 + \vec{\nabla}\cdot(\alpha_1 \vec{u}) = \frac{\mathcal{M}}{\rho_1}\,, \tag{33a}$$

$$\partial_t(\alpha_2\rho_2) + \vec{\nabla}\cdot(\alpha_2\rho_2\vec{u}) = -\mathcal{M}\,. \tag{33b}$$

The equations for the gas partial densities $\rho_v = \rho_2\xi$ and $\rho_a = \rho_2(1-\xi)$ are:

$$\partial_t(\alpha_2\rho_2\xi) + \vec{\nabla}\cdot(\alpha_2\rho_2\xi\vec{u}) = -\mathcal{M} + \vec{\nabla}\cdot(\alpha_2\rho_2 D_{va}\vec{\nabla}\xi)\,, \tag{34a}$$

$$\partial_t(\alpha_2\rho_2(1-\xi)) + \vec{\nabla}\cdot(\alpha_2\rho_2(1-\xi)\vec{u}) = \vec{\nabla}\cdot(\alpha_2\rho_2 D_{va}\vec{\nabla}(1-\xi))\,, \tag{34b}$$

where we have also included the binary mass diffusion term $\vec{\nabla}\cdot(\alpha_2\rho_2 D_{va}\vec{\nabla}\xi)$ with a diffusion coefficient D_{va}. Concerning the equation for the mixture enthalpy (ρh) in (22e), since we assume that phase 1 is incompressible, we multiply the term $\frac{dp_0}{dt}$ by α_2 for the

consistency of the model, and to recover the correct limit in the incompressible liquid region (where $\vec{\nabla}\cdot\vec{u}=0$). Indeed the derivation in the low-Mach number limit of the equation for (ρh) in (21e) from the equation (18e) holds if $K_{Sk}=\frac{1}{\rho_k c_k^2}\neq 0$, $k=1,2$, while we have $K_{S1}=0$ if phase 1 is incompressible. Therefore we now write:

$$\partial_t(\rho h)+\vec{\nabla}\cdot(\rho h\vec{u})=\vec{\nabla}\cdot(\lambda_c\vec{\nabla}T)+\alpha_2\frac{dp_0(t)}{dt}\,. \tag{35}$$

We will see that this form of the equation is consistent with the equation for $\vec{\nabla}\cdot\vec{u}$ (Appendix B). Concerning the equation for $\vec{\nabla}\cdot\vec{u}$, see (22d), we write it here for the specific case of incompressible liquid, and, moreover, we extend it to the case in which the gaseous phase is a two-component ideal gas mixture with vapor mass fraction ξ, this implying also an additional binary diffusion contribution in the constraint for the divergence of the velocity field, $\vec{\nabla}\cdot\vec{u}$. We derive the equation for $\vec{\nabla}\cdot\vec{u}$ by starting from the equation for ρ:

$$\vec{\nabla}\cdot\vec{u}=-\frac{1}{\rho}\frac{D\rho}{Dt}=\frac{1}{v}\frac{Dv}{Dt}\,, \tag{36}$$

where $\frac{D}{Dt}=\frac{\partial}{\partial t}+\vec{u}\cdot\vec{\nabla}$, and $v=1/\rho$. We obtain:

$$\vec{\nabla}\cdot\vec{u}=\bar{Z}\mathcal{M}+\bar{B}\,\vec{\nabla}\cdot(\lambda_c\vec{\nabla}T)+\bar{D}\mathcal{D}-\bar{K}_S\frac{dp_0(t)}{dt}\,, \tag{37}$$

where we have denoted $\mathcal{D}=\vec{\nabla}\cdot(\alpha_2\rho_2 D_{va}\vec{\nabla}\xi)$, and

$$\bar{Z}=\left(\frac{1}{\rho_1}-\frac{1}{\rho_2}\right)-(1-\xi)\frac{M_2(\xi)}{\rho_2}\left(\frac{1}{M_v}-\frac{1}{M_a}\right)+\frac{\alpha_2(h_v-h_1)}{T\rho(Y_1\kappa_{p1}+Y_2\kappa_{p2}(\xi))}, \tag{38a}$$

$$\bar{D}=\frac{M_2(\xi)}{\rho_2}\left(\frac{1}{M_v}-\frac{1}{M_a}\right)+\frac{\alpha_2(h_a-h_v)}{T\rho(Y_1\kappa_{p1}+Y_2\kappa_{p2}(\xi))}, \tag{38b}$$

$$\bar{B}=\frac{\alpha_2}{T\rho(Y_1\kappa_{p1}+Y_2\kappa_{p2}(\xi))}, \tag{38c}$$

$$\bar{K}_S=\alpha_2\left(\frac{1}{p_0}-\frac{\alpha_2}{T\rho(Y_1\kappa_{p1}+Y_2\kappa_{p2}(\xi))}\right)=\frac{\alpha_2\left(\alpha_1\rho_1\kappa_{p1}+\alpha_2\rho_2\frac{\kappa_{p2}(\xi)}{\gamma_2(\xi)}\right)}{p_0(\alpha_1\rho_1\kappa_{p1}+\alpha_2\rho_2\kappa_{p2}(\xi))}. \tag{38d}$$

Note that in the expressions above we can write $\rho(Y_1\kappa_{p1}+Y_2\kappa_{p2}(\xi))=\alpha_1\rho_1\kappa_{p1}+\alpha_2\rho_2\kappa_{p2}(\xi)$. The derivation of (37)-(38) is shown in Appendix A. Moreover, in Appendix B we will show that this expression for $\vec{\nabla}\cdot\vec{u}$ is in agreement with (22d).

We finally consider the following augmented formulation of the model:

$$\partial_t\alpha_1+\vec{\nabla}\cdot(\alpha_1\vec{u})=\frac{\mathcal{M}}{\rho_1}\,, \tag{39a}$$

$$\partial_t(\alpha_2\rho_2)+\vec{\nabla}\cdot(\alpha_2\rho_2\vec{u})=-\mathcal{M}\,, \tag{39b}$$

$$\partial_t(\alpha_2\rho_2\xi)+\vec{\nabla}\cdot(\alpha_2\rho_2\xi\vec{u})=-\mathcal{M}+\vec{\nabla}\cdot(\alpha_2\rho_2 D_{va}\vec{\nabla}\xi)\,, \tag{39c}$$

$$\partial_t(\rho\vec{u})+\vec{\nabla}\cdot(\rho\vec{u}\otimes\vec{u})+\vec{\nabla}\tilde{p}=\vec{\nabla}\cdot\vec{\bar{\tau}}+\vec{\Sigma}+\rho\vec{g}\,, \tag{39d}$$

$$\vec{\nabla}\cdot\vec{u}=\bar{Z}\mathcal{M}+\bar{B}\,\vec{\nabla}\cdot(\lambda_c\vec{\nabla}T)+\bar{D}\vec{\nabla}\cdot(\alpha_2\rho_2 D_{va}\vec{\nabla}\xi)-\bar{K}_S\frac{dp_0(t)}{dt}\,, \tag{39e}$$

$$\partial_t(\rho h)+\vec{\nabla}\cdot(\rho h\vec{u})=\vec{\nabla}\cdot(\lambda_c\vec{\nabla}T)+\alpha_2\frac{dp_0(t)}{dt}\,, \tag{39f}$$

where the mixture quantities $\bar{K}_S$, $\bar{B}$, $\bar{Z}$, $\bar{D}$ are defined in (38a), (38b), (38c), (38d). Let us remark that the mass transfer term $\mathcal{M}$ is defined only in the mixture region, $0<\alpha_1<1$. This can be automatically obtained by a suitable definition of $\mathcal{M}$ (see for example (53)).

When solving the system above, we can obtain the mixture specific enthalpy h once α_1, $m_2\equiv\alpha_2\rho_2$, and ρh have been computed. The temperature T is then obtained from $h=Y_1h_1+Y_2(\xi h_v+(1-\xi)h_a)$, once ξ is known:

$$T=\frac{h-Y_1\eta_1-Y_2\eta_2}{Y_1\kappa_{p1}+Y_2(\xi\kappa_{pv}+(1-\xi)\kappa_{pa})}\,, \tag{40}$$

where for h_1 we have used the enthalpy law in (24), whereas for h_2 we have used the slightly more general law $h_2=\kappa_{p2}T+\eta_2$, $\eta_2=$ constant (in (30) $\eta_2=0$). We can also express T directly in terms of the primary variables (ρh) and m_2 of the augmented model (39):

$$T=\frac{\rho h-\alpha_1\rho_1\eta_1-\alpha_2\rho_2\eta_2}{\alpha_1\rho_1\kappa_{p1}+m_2(\xi\kappa_{pv}+(1-\xi)\kappa_{pa})}\,. \tag{41}$$

Finally, the thermodynamics pressure can be obtained by

$$\frac{dp_0(t)}{dt}=-\frac{1}{A}\int_{\partial\Omega}\vec{u}\cdot\vec{n}\,dS+\frac{1}{A}\int_{\Omega}\bar{B}\vec{\nabla}\cdot(\lambda_c\vec{\nabla}T)\,dV+\frac{1}{A}\int_{\Omega}\bar{D}\mathcal{D}\,dV+\frac{1}{A}\int_{\Omega}\bar{Z}\mathcal{M}\,dV,\quad A=\int_{\Omega}\bar{K}_S\,dV. \tag{42}$$

2.4. Mass transfer term

The mass transfer between the liquid phase (denoted with 1) and the vapor phase (denoted with v) is driven by the difference of the chemical potentials μ_1^p and μ_v^p of these phases, hence it can be expressed as a relaxation term depending on this difference (see e.g. [95,96,63,97,98]):

$$\mathcal{M} = \frac{1}{\Omega_\mu \tau}(\mu_v^p - \mu_1^p), \tag{43}$$

where $\tau \geq 0$ is a relaxation time, and $\Omega_\mu > 0$ is a parameter or function. A definition must be provided for the relaxation rate $\frac{1}{\Omega_\mu \tau}$ where instantaneous mass transfer corresponds to $\tau \to 0^+$. The liquid is pure, so its chemical potential is equal to its Gibbs free energy, $\mu_1^p = g_1(p,T)$, and it is also assumed incompressible, so that the chemical potential can be written as (see for instance [99]):

$$\mu_1^p = g_1(p,T) = g_1(p_{\text{sat}}(T),T) + \frac{1}{\rho_1}[p - p_{\text{sat}}(T)], \tag{44}$$

where $p_{\text{sat}}(T)$ is the saturation pressure-temperature law of the pure constituent that undergoes liquid-vapor transition. The chemical potential of the vapor depends on the molar fraction X_v of the vapor in the ideal gas mixture:

$$\mu_v^p = g_v(p,T) + \frac{\mathcal{R}}{M_v} T \log X_v\,, \tag{45}$$

where the Gibbs free energy $g_v(p,T)$ of the vapor can be expressed as

$$g_v(p,T) = g_v(p_{\text{sat}}(T),T) + \frac{\mathcal{R}}{M_v} T \log \frac{p}{p_{\text{sat}}(T)}\,. \tag{46}$$

By using the relation $g_1(p_{\text{sat}}(T),T) = g_v(p_{\text{sat}}(T),T)$, the difference of the chemical potentials can be written as

$$\Delta\mu^p = \mu_v^p(p,T,X_v) - \mu_1^p(p,T) = \frac{\mathcal{R}}{M_v} T \log \frac{p}{p_{\text{sat}}(T)} + \frac{\mathcal{R}}{M_v} T \log X_v - \frac{1}{\rho_1}[p - p_{\text{sat}}(T)] \tag{47a}$$

$$= \frac{\mathcal{R}}{M_v} T \log \frac{pX_v}{p_{\text{sat}}(T)} - \frac{1}{\rho_1}[p - p_{\text{sat}}(T)]\,. \tag{47b}$$

The thermodynamic equilibrium is defined by the equality $\mu_1^p(p,T) = \mu_v^p(p,T,X_v) \Leftrightarrow \Delta\mu^p = 0$. Note that the vapor molar fraction X_v and the vapor mass fraction ξ are linked through the relations:

$$X_v = \frac{\xi}{\xi + (1-\xi)\frac{M_v}{M_a}}\,, \qquad \xi = \frac{X_v}{X_v + (1-X_v)\frac{M_a}{M_v}}\,. \tag{48}$$

We could make an approximation and neglect the liquid specific volume $\frac{1}{\rho_1}$ with respect to the vapor specific volume [99], $\frac{1}{\rho_1} \ll \frac{1}{RT} p_{\text{sat}}(T) R_v$. Then relation (47) becomes:

$$\Delta\mu^p = \frac{\mathcal{R}}{M_v} T \log \frac{pX_v}{p_{\text{sat}}(T)}, \tag{49}$$

and imposing the equilibrium $\Delta\mu^p = 0$ gives

$$X_{v,\text{sat}} = \frac{p_{\text{sat}}(T)}{p}\,, \tag{50}$$

which allows us to express the equilibrium vapor molar fraction X_v and hence the vapor mass fraction ξ as a function of the saturation pressure and the reference pressure. This suggests another possible expression for the mass transfer term $\mathcal{M}$, which is based on the relaxation of the vapor mass fraction with a relaxation time τ_ξ:

$$\mathcal{M} = \frac{1}{\Omega_\xi \tau_\xi}(\xi - \xi_{\text{sat}}), \tag{51}$$

with

$$\xi_{\text{sat}} = \frac{X_{v,\text{sat}}}{X_{v,\text{sat}} + (1 - X_{v,\text{sat}})\frac{M_a}{M_v}} = \frac{p_{\text{sat}}(T)}{p_{\text{sat}}(T) + (p - p_{\text{sat}}(T))\frac{M_a}{M_v}}\,, \tag{52}$$

where we have used (50), and $\frac{1}{\Omega_\xi \tau_\xi}$ expresses the relaxation rate. In particular, we will adopt the following expression that vanishes in pure liquid and pure gaseous regions:

$$\mathcal{M} = \frac{\alpha_1 \alpha_2 (\alpha_2 \rho_2)}{\tau_\xi}(\xi - \xi_{\text{sat}})\,, \tag{53}$$

and we employ Antoine equation to define the function $p_{\text{sat}}(T)$,

$$\log_{10} p = A_A - \frac{B_A}{C_A + T}, \tag{54}$$

where A_A, B_A, C_A are empirical coefficients. A similar expression of the mass transfer is used for instance in [45]. We finally recall that the thermodynamic pressure p to be used in the above expressions is $p = p_0(t)$.

2.5. Multicomponent liquid-vapor-gas model with incompressible gases

We present a variant of the liquid-vapor-gas model with mass transfer based on a different mixture model for the gaseous phase with respect to the model in the previous section, this also showing how the more general model presented in this work recovers the model in [45] when the same assumptions are made. The liquid (phase 1) is still considered incompressible, but here each component of the vapor-gas mixture (gaseous phase 2) is assumed to occupy its own volume, i.e. $V_2 = V_v + V_a$. We therefore assume (instead of (27)):

$$v_2 = v_v \xi + v_a (1 - \xi), \tag{55}$$

where $v = \frac{1}{\rho}$ denotes the specific volume, and, as before, ξ the vapor mass fraction $\xi = \mathrm{m}_v / \mathrm{m}_2$ in the gaseous phase. The mixture specific enthalpy h_2 and specific energy ε_2 can be expressed as in (28) (but relations (29) do not hold any longer). Additionally, we assume that the densities $\rho_v = \mathrm{m}_v / V_v$ and $\rho_a = \mathrm{m}_a / V_a$ are constant (incompressible gases). The specific enthalpies are assumed to obey the ideal gas laws $h_v = \kappa_{pv} T$ and $h_a = \kappa_{pa} T$. Hence, as in the previous model, for the mixture

$$h_2 = \kappa_2 T, \quad \kappa_2(\xi) = \kappa_{pv} \xi + \kappa_{pa} (1 - \xi). \tag{56}$$

Concerning the model equations, clearly the equations for the volume fraction α_1 in (39a), the equation for the partial density $\alpha_2 \rho_2$ in (39b), and the equation for the vapor mass fraction ξ either in the form in (A.6) (for ξ) or in the form in (39c) (for $\alpha_2 \rho_2 \xi$) hold. The enthalpy equation is given by equation (39f) with $dp_0/dt = 0$ (due to the assumption of liquid and gases incompressibility). We can now derive the divergence constraint, using the equation for ρ as for the model of the previous section:

$$\vec{\nabla} \cdot \vec{u} = -\frac{1}{\rho} \frac{D\rho}{Dt} = \frac{1}{v} \frac{Dv}{Dt}. \tag{57}$$

Thus, we obtain

$$\vec{\nabla} \cdot \vec{u} = \bar{Z} \mathcal{M} + \bar{D} D, \tag{58}$$

where

$$\bar{Z} = \frac{1}{\rho_1} - \frac{1}{\rho_v}, \qquad \bar{D} = \frac{1}{\rho_v} - \frac{1}{\rho_a}, \tag{59}$$

and $\mathcal{D} = \vec{\nabla}(\alpha_2 \rho_2 D_{va} \vec{\nabla} \xi)$ the mass diffusion term, same as before. Here, in contrast to the model in Section 2.3, we do not use an augmented formulation of the model with an additional mass equation since the gas densities are constant. The model system can be written as:

$$\partial_t \alpha_1 + \vec{\nabla} \cdot (\alpha_1 \vec{u}) = \frac{\mathcal{M}}{\rho_1}, \tag{60a}$$

$$\partial_t (\alpha_2 \rho_2 \xi) + \vec{\nabla} \cdot (\alpha_2 \rho_2 \xi \vec{u}) = -\mathcal{M} + \vec{\nabla} \cdot (\alpha_2 \rho_2 D_{va} \vec{\nabla} \xi), \tag{60b}$$

$$\partial_t (\rho \vec{u}) + \vec{\nabla} \cdot (\rho \vec{u} \otimes \vec{u}) + \vec{\nabla} \tilde{p} = \vec{\nabla} \cdot \vec{\tau} + \vec{\Sigma} + \rho \vec{\mathrm{g}}, \tag{60c}$$

$$\vec{\nabla} \cdot \vec{u} = \bar{Z} \mathcal{M} + \bar{D} \vec{\nabla} \cdot (\alpha_2 \rho_2 D_{va} \vec{\nabla} \xi), \tag{60d}$$

$$\partial_t (\rho h) + \vec{\nabla} \cdot (\rho h \vec{u}) = \vec{\nabla} \cdot (\lambda_c \vec{\nabla} T), \tag{60e}$$

with $\bar{Z}$ and $\bar{D}$ defined in eq. (59). Comparing with the model in Ref. [45], we have also a contribution from the mass diffusion term, $\mathcal{D}$ in the equation for $\vec{\nabla} \cdot \vec{u}$ (the contribution $\bar{D} D$ due to changes in density related to composition); this is neglected in [45], and in the present computations, due to its minimal contribution.

2.5.1. Mass transfer

The model for mass transfer presented in Section 2.4 is based on the assumption of a mixture of ideal gases obeying to Dalton's law, whereas we are now working with multicomponent model with constant densities. Nonetheless, following [45] we could still use the expression for mass transfer $\mathcal{M}$ in (51) or (53) based on a relaxation term for the vapor mass fraction ξ, since the expression for the equilibrium mass fraction ξ_{eq} in (52) involves only the temperature T (via the function $p_{\mathrm{sat}}(T)$), and the molar weights of the gases. The pressure p corresponds to the thermodynamic pressure p_0.

2.6. Model with interface sharpening

As discussed by several authors, one drawback of diffuse interface models is the numerical diffusion of the mixture region. To overcome this issue, we follow the works of [54,100] and propose a formulation of the diffuse interface liquid-vapor-gas models just introduced with regularization terms for interface re-sharpening. The more general model in equation (39) with regularization terms becomes:

$$\partial_t \alpha_1 + \vec{\nabla}\cdot(\alpha_1\vec{u}) = \frac{\mathcal{M}}{\rho_1} + \vec{\nabla}\cdot\vec{r}_1\,, \tag{61a}$$

$$\partial_t(\alpha_2\rho_2) + \vec{\nabla}\cdot(\alpha_2\rho_2\vec{u}) = -\mathcal{M} + \vec{\nabla}\cdot(\rho_2\vec{r}_2)\,, \tag{61b}$$

$$\partial_t(\alpha_2\rho_2\xi) + \vec{\nabla}\cdot(\alpha_2\rho_2\xi\vec{u}) = -\mathcal{M} + \vec{\nabla}\cdot(\alpha_2\rho_2 D_{va}\vec{\nabla}\xi) + \vec{\nabla}\cdot(\rho_2\xi\vec{r}_2)\,, \tag{61c}$$

$$\partial_t(\rho\vec{u}) + \vec{\nabla}\cdot(\rho\vec{u}\otimes\vec{u} - ((\rho_1\vec{r}_1 + \rho_2\vec{r}_2)\otimes\vec{u})) + \vec{\nabla}\tilde{p} = \vec{\nabla}\cdot\vec{\tilde{\tau}} + \vec{\Sigma} + \rho\vec{\mathfrak{g}}\,, \tag{61d}$$

$$\vec{\nabla}\cdot\vec{u} = \bar{Z}\mathcal{M} + \bar{B}\,\vec{\nabla}\cdot(\lambda_c\vec{\nabla}T) + \bar{D}\vec{\nabla}\cdot(\alpha_2\rho_2 D_{va}\vec{\nabla}\xi) - \bar{K}_S\frac{dp_0(t)}{dt}\,, \tag{61e}$$

$$\partial_t(\rho h) + \vec{\nabla}\cdot(\rho h\vec{u} - (\rho_1 h_1\vec{r}_1 + \rho_2 h_2\vec{r}_2)) = \vec{\nabla}\cdot(\lambda_c\vec{\nabla}T)\,. \tag{61f}$$

Above $\vec{r}_k$, $k = 1, 2$, are regularization quantities that we express here as in [54]:

$$\vec{r}_k = \Xi\left[\epsilon_I\,\vec{\nabla}\alpha_k - \alpha_1(1-\alpha_1)\vec{n}_1\right], \qquad \vec{n}_1 = \frac{\vec{\nabla}\alpha_1}{|\vec{\nabla}\alpha_1|}, \quad k = 1, 2, \tag{62}$$

with ϵ_I denoting the interface thickness, and Ξ the regularization velocity (these parameters need to be chosen to satisfy criteria for boundedness [54]). Note that $\vec{r}_2 = -\vec{r}_1$, hence the regularization terms in the momentum and enthalpy equations can be rewritten as:

$$\vec{\nabla}\cdot((\rho_1\vec{r}_1 + \rho_2\vec{r}_2)\otimes\vec{u}) = \vec{\nabla}\cdot((\rho_1 - \rho_2)\vec{r}_1\otimes\vec{u})\,, \tag{63a}$$

$$\vec{\nabla}\cdot(\rho_1 h_1\vec{r}_1 + \rho_2 h_2\vec{r}_2) = \vec{\nabla}\cdot((\rho_1 h_1 - \rho_2 h_2)\vec{r}_1)\,. \tag{63b}$$

The model assuming constant density of the two gaseous components, see equations (60), has analogous interface regularization terms in the equations for α_1, $\alpha_2\rho_2\xi$, $\rho\vec{u}$ and ρh, and it takes the form:

$$\partial_t \alpha_1 + \vec{\nabla}\cdot(\alpha_1\vec{u}) = \frac{\mathcal{M}}{\rho_1} + \vec{\nabla}\cdot\vec{r}_1\,, \tag{64a}$$

$$\partial_t(\alpha_2\rho_2\xi) + \vec{\nabla}\cdot(\alpha_2\rho_2\xi\vec{u}) = -\mathcal{M} + \vec{\nabla}\cdot(\alpha_2\rho_2 D_{va}\vec{\nabla}\xi) + \vec{\nabla}\cdot(\rho_2\xi\vec{r}_2)\,, \tag{64b}$$

$$\partial_t(\rho\vec{u}) + \vec{\nabla}\cdot(\rho\vec{u}\otimes\vec{u} - ((\rho_1\vec{r}_1 + \rho_2\vec{r}_2)\otimes\vec{u})) + \vec{\nabla}\tilde{p} = \vec{\nabla}\cdot\vec{\tilde{\tau}} + \vec{\Sigma} + \rho\vec{\mathfrak{g}}\,, \tag{64c}$$

$$\vec{\nabla}\cdot\vec{u} = \bar{Z}\mathcal{M} + \bar{D}\vec{\nabla}\cdot(\alpha_2\rho_2 D_{va}\vec{\nabla}\xi)\,, \tag{64d}$$

$$\partial_t(\rho h) + \vec{\nabla}\cdot(\rho h\vec{u} - (\rho_1 h_1\vec{r}_1 + \rho_2 h_2\vec{r}_2)) = \vec{\nabla}\cdot(\lambda_c\vec{\nabla}T)\,, \tag{64e}$$

Let us remark that the equation for the vapor mass fraction (61b) and (64b) in the incompressible flow case corresponds to the consistent formulation for scalar transport in multiphase flows proposed in [101].

3. Numerical solution method

The final set of equations (61) describes a flow composed of a liquid phase and gaseous weakly compressible components in the limit of low Mach number whereas the equations (64) describe a flow with incompressible components. Both systems of equations are solved on a Cartesian regular grid with uniform grid spacing in the three directions: x, y, and z. The spacing along x is calculated as $\Delta x = l_x/N_x$, where l_x is the domain dimension and N_x is the number of grid cells in the x direction. Similar definitions are used for the y and z directions. We employ a finite-volume discretization strategy on a staggered grid, where the phase field, pressure, vapor mass fraction, and scalar fields (such as density, viscosity, thermal conductivity) are located at the cell centers, and the components of the velocity field vector are positioned at the cell faces where all the fluxes are evaluated. This discretization method is chosen to prevent the spurious checkerboarding of the pressure field [102]. We utilize a two-fluid Navier-Stokes solver that incorporates a projection method [103] and a pressure-splitting technique [47] to simplify the variable coefficient pressure Poisson equation to a constant coefficient equation. This adaptation enables the use of an FFT-based, fast Poisson solver, which is approximately one order of magnitude faster than a standard iterative solver [104]. Nonetheless, our numerical model is adaptable to any conventional two-fluid solvers without the necessity of employing the pressure-splitting technique.

We employ the second-order Adams-Bashforth scheme for temporal discretization and the second-order central-difference scheme for spatial operator discretization. This choice of numerical schemes offers advantages such as a non-dissipative nature, low cost, and improved stability [105]. By appropriately selecting Δt (time-step size), Ξ, and ϵ, we ensure positivity in the vapor concentration field and maintain the boundedness and Total Variation Diminishing (TVD) properties of the phase field (which results in the boundedness of the density field) [106]. The advantage also stems from the fact that transporting mass flux in the convective term of the momentum equation (61d) is consistent at the discrete level with the advective flux in the phase field equation (61a), details of which are discussed

further in [107]. In Appendix D, we present the pseudo-algorithm of our numerical scheme, detailing all spatial discretization choices, using for simplicity first-order explicit temporal discretization.

To maintain the boundedness and TVD properties of the phase field, we follow the criteria provided by [54] for simulating two-phase compressible flows, which are as follows:

$$\Delta t \leq \min_i \left[\frac{1}{\max\left\{ \left(\frac{2D_f \Xi \epsilon}{\Delta x^2} \right) - \left(\frac{\partial u_i}{\partial x_i} \right), 0 \right\}} \right], \tag{65a}$$

$$\left(\frac{2D_f \Xi \epsilon}{\Delta x^2} \right) \geq \max_i \left\{ \left(\frac{\partial u_i^k}{\partial x_i} \right) \right\}, \tag{65b}$$

$$\frac{\epsilon}{\Delta x} \geq \frac{\left(\frac{|\vec{u}|_{\max}}{\Xi} + 1 \right)}{2}, \tag{65c}$$

where D_f represents the number of dimensions, $\delta/\delta x$ is the discrete derivative operator, i is the grid index, k represents the time-step index, and $|\vec{u}|_{\max}$ is the maximum velocity in the domain. For incompressible flows, the TVD condition (eq. (65)(b)) is always trivially satisfied, and the time-step restriction required for the boundedness of the phase field (eq. (65)(a)) simplifies to $\Delta t \leq \Delta x^2/(2D_f\epsilon)$. However, for compressible flows with a non-solenoidal velocity field, the time-step condition depends on the local dilation of the flow. For all the simulations in this work, we used $\Xi = |\vec{u}|_{\max}$, $\epsilon = \Delta x$, and a time-step size determined by the CFL condition, along with the maximum allowable time scales given in eq. (67). These choices were sufficient to ensure the boundedness and TVD properties of the phase field.

For each test case, the relaxation time-scale τ_ξ is scaled with the smallest time-scale of the system throughout the simulations, following [45]:

$$\tau_\xi = \min(\tau_c, \tau_\mu, \tau_D, \tau_e, \tau_{\mathcal{M}}), \tag{66}$$

where τ_c, τ_μ, τ_D, τ_e and $\tau_{\mathcal{M}}$ are the maximum allowable time-scales due to convection, momentum diffusion, vapor mass diffusion, thermal diffusion and phase change. These are determined as:

$$\tau_c = \left(\frac{|u_{x,max}|}{\Delta x} + \frac{|u_{y,max}|}{\Delta y} + \frac{|u_{z,max}|}{\Delta z} \right)^{-1}, \tag{67a}$$

$$\tau_\mu = \left[\max\left(\frac{\mu_1}{\rho_1}, \frac{\mu_2}{\rho_2} \right) \left(\frac{2}{\Delta x^2} + \frac{2}{\Delta y^2} + \frac{2}{\Delta z^2} \right) \right]^{-1}, \tag{67b}$$

$$\tau_D = \left[D_{va} \left(\frac{2}{\Delta x^2} + \frac{2}{\Delta y^2} + \frac{2}{\Delta z^2} \right) \right]^{-1}, \tag{67c}$$

$$\tau_e = \left[\max\left(\frac{\lambda_{c1}}{\rho_1 \kappa_{p1}}, \frac{\lambda_{c2}}{\rho_2 \kappa_{p2}} \right) \left(\frac{2}{\Delta x^2} + \frac{2}{\Delta y^2} + \frac{2}{\Delta z^2} \right) \right]^{-1}, \tag{67d}$$

$$\tau_{\mathcal{M}} = \frac{\rho_2}{|\mathcal{M}_{max}|}, \tag{67e}$$

where $|u_{i,\max}|$ represents the maximum estimate of the ith component of the flow velocity, and $|\mathcal{M}_{\max}|$ denotes the maximum local value of the source term responsible for the phase change. The same strategy has been employed to determine the required Δt for stable time integration.

4. Numerical validation tests

In this section, we examine the validation of the proposed numerical model by assessing its performance against various benchmark cases. To enhance clarity, we have summarized the physical and thermophysical parameters defining each setup in Table 3. Below we present the relevant non-dimensional parameters, obtained using appropriate scaling factors: a reference velocity (u_{ref}), length (l_{ref}), and temperature (T_{ref}), along with the reference thermophysical properties, which are taken from gas phase 2,

$$\text{Re} = \frac{\rho_2 u_{ref} l_{ref}}{\mu_2}, \quad \text{We} = \frac{\rho_2 u_{ref}^2 l_{ref}}{\sigma}, \quad \text{Fr} = \frac{u_{ref}^2}{l_{ref}|\vec{g}|}, \quad \text{Pr} = \frac{\mu_2 \kappa_{p2}}{\lambda_{c2}}, \quad \text{Sc} = \frac{\mu_2}{D_{va}\,\rho_2},$$

$$\text{Ste} = \frac{\kappa_{p2} T_{ref}}{L_{\text{lat}}}, \quad r_\Lambda \equiv \frac{\Lambda_1}{\Lambda_2}.$$

Table 3
Governing parameters for the cases presented in this section. For all cases $l_{ref} = d_0$ where d_0 is the initial droplet diameter. $T_{g,0}$ denotes the initial gas temperature.

Sec.	Re	We	Fr	Pr	Sc	Ste	r_ρ	r_μ	r_{κ_p}	r_{λ_c}	r_M	u_{ref}	T_{ref}
4.1.1	25	0.1	∞	N/A	0.8	N/A	$10-1000$	50	N/A	N/A	N/A	D_{va}/d_0	N/A
4.1.2	1.5	0.02	∞	0.7	0.06	var	8.33	63.6	4.16	0.230	0.62	D_{va}/d_0	$T_{sat}-T_\infty$
4.1.3	13.3	1.10	1	0.15	var	0.13	$10-1000$	20	4.16	0.232	0.62	$\sqrt{\lvert\vec{g}\rvert d_0}$	$T_{g,0}$
4.2.1	10	1.0	∞	0.77	0.1	0.03	8.33	50	4.16	0.230	0.62	D_{va}/d_0	$T_{sat}-T_\infty$
4.2.2	90	0.5	1	0.1	0.065	0.17	10	50	4	2.5	0.62	$\sqrt{\lvert\vec{g}\rvert d_0}$	$T_{g,0}$

In the expression above, Re, We, Fr, Pr, Sc, Ste, and r_Λ are the Reynolds, Weber, Froude, Prandtl, Schmidt, Stefan number, and the ratio of the different thermophysical properties, r_Λ, where the property Λ can be ρ, μ, κ_p, λ_c or the molar mass. In section 4.1, we assume that all the thermophysical properties, including phase density, are uniform and constant within both the gas-phase (i.e. we assume the vapor phase has the same thermophysical properties as the inert gas) and liquid-phase. In contrast, for the case in section 4.2 we assume that the thermophysical properties of the liquid-phase remain uniform and constant, whereas those of the gas-phase vary with composition, temperature, and thermodynamic pressure.

4.1. Incompressible gas phase & incompressible liquid phase

In this section, both phases are assumed to be incompressible, and their thermophysical properties are considered constant and uniform. Based on these assumptions, we solve the system of equations described in Section 2.5.

4.1.1. Isothermal evaporation

In this section, we examine the isothermal evaporation of a two-dimensional circular droplet to validate the numerical method for simulating phase-changing two-fluid flows, decoupled from the enthalpy transport equation. The circular droplet is positioned within a square domain of size $[-2d_0, 2d_0]^2$, where d_0 denotes the initial droplet diameter, with zero-pressure outflow boundaries. The concentration difference between the droplet interface and the domain boundary drives evaporation. Therefore, we solve eq. (60b) with zero-Dirichlet boundary conditions (hence, $\xi_\infty = 0$) at the domain boundaries, while enforcing $\xi_{sat} = 0.5$. The mass transfer ($\mathcal{M}$) is then computed from eq. (53) where $\alpha_2 = 1 - \alpha_1$. This allows us to assess the method accuracy for coupling the vapor mass fraction transport to Navier-Stokes equations, decoupled from the enthalpy equation. The physical parameters used in this study are detailed in Table 3; in particular, we examine three different density ratios, $r_\rho = \{10, 100, 1000\}$, keeping the other parameters fixed. The steady solution of eq. (60b) with $\vec{u} = 0$ is used as the initial condition for ξ.

For this system, the time evolution of the droplet diameter d for two-dimensional two-component isothermal evaporation can be described by the following analytical expression [108]:

$$(\ln(L/d) + 1/2)d^2 = (\ln(L/d_0) + 1/2)d_0^2 - Kt. \tag{68}$$

Here, $K = (8\rho_2 D_{va}/\rho_1)\ln(1+B)$ with $B = (\xi_{sat} - \xi_\infty)/(1 - \xi_{sat}) = 0.5$, and $L = 4d_0$ represents the diameter of a circular domain. The equation above is solved numerically to provide a reference solution for the temporal evolution of droplet diameter, $d(t)$.

Fig. 1(a) depicts the normalized vapor mass fraction field for the case of $r_\rho = 1000$ evaluated at the highest resolution (256×256). This field is used to calculate the interfacial mass transfer, as reported in Fig. 1(b), which is only defined in the region where $0 < \alpha_1 < 1$. Additionally, the Stefan flow due to phase change is illustrated in Fig. 1(b) using the velocity vector field. The proposed approach yields consistent numerical solution in terms of mass and droplet volume conservation compared to the analytical solution, as demonstrated below.

Fig. 2 depicts the temporal evolution of the normalized droplet diameter, derived from its volume (i.e., in a two-dimensional configuration, $d = \sqrt{4A/\pi}$ where A is the surface area). This is illustrated for various values of the density ratio, r_ρ. Additionally, grid convergence studies are conducted for the three distinct density ratios. The results demonstrate excellent agreement between the Direct Numerical Simulation (DNS) results and the analytical solution across a range of r_ρ, including high-density ratios. As expected, we note a slight deviation from the analytical solution when the number of grid points per droplet diameter has significantly decreased, due to substantial vaporization of the droplet. Fig. 3 presents the convergence of the numerical error with grid refinement for the case with the highest density ratio (i.e. $r_\rho = 1000$), obtained with fixed time step $\Delta t = 10^{-6} d_0^2 / D_{va}$ and $d/d_0 = 0.5$. The results demonstrate that the convergence rate is approximately 1.69.

4.1.2. Thermal evaporation

In this case, the enthalpy transport equation is coupled to the conservation of mass and momentum for the same configuration as the previous case. Here, evaporation is driven by the partial pressure of the vaporized liquid at the interface, which is lower than the saturated pressure at the interface, denoted as p_{sat}. The saturated pressure at the interface is related to the interface temperature through the Antoine equation. A stationary, two-dimensional circular droplet with the same geometry and outflow conditions as before is considered. The enthalpy equation is solved using Dirichlet boundary conditions at all boundaries in order to impose $T_\infty = T_{db}$ at all boundaries, where T_{db} denotes dry bulb temperature. The steady-state solution of the vapor mass fraction equation with ($\vec{u} = 0$) serves as the initial condition for the vapor mass fraction (ξ), with Dirichlet boundary conditions (ξ_∞) at the domain boundaries. The

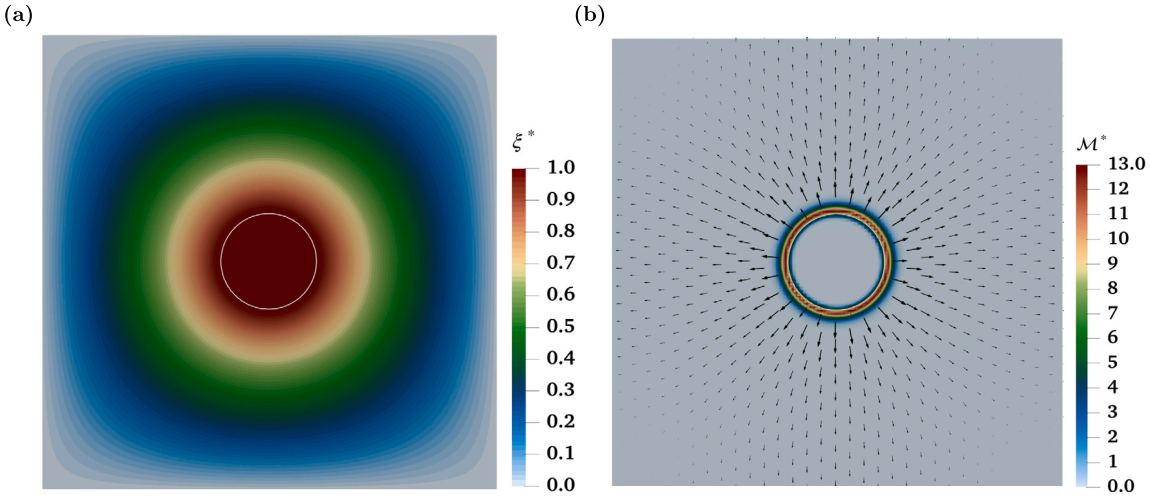

Fig. 1. Isothermal evaporation of a static two-dimensional droplet. (a): Contours of the normalized vapor mass fraction field $\xi^* = (\xi - \xi_\infty)/(\xi_{sat} - \xi_\infty)$; (b): contours of the dimensionless interfacial mass transfer $\mathcal{M}^* = (\mathcal{M} d_0^2)/(\rho_2 D_{va})$ at $t D_{va}/d_0^2 = 79.48$. The approximate interface location ($\alpha_1 = 0.5$) is depicted by the solid white line.

vapor saturation value (ξ_{sat}) is calculated from the Antoine relation. Psychrometric data is used to validate the numerical method, similar to previous studies [25,13]. In this scenario, a water droplet is placed in air with a relative humidity ψ and an initial dry bulb temperature T_{db}, equal to the initial droplet temperature. Upon evaporation, the droplet cools and its temperature drops. This cooling is counterbalanced by conductive heat flux from the warmer air to the droplet, leading to an equilibrium temperature within the droplet, known as the wet-bulb temperature T_{wb}. The mass fraction at the boundary ξ_∞ is calculated based on the desired air relative humidity ψ at T_{db}:

$$\xi_\infty = \frac{\psi\, p_\infty^{sat}\, M_v}{(\,p - \psi\, p_\infty^{sat}\,)M_a + \psi\, p_\infty^{sat}\, M_v}, \tag{69}$$

with p_∞^{sat} computed from the Antoine relation evaluated at T_{db}.

Fig. 4(a) shows the time evolution of the droplet temperature profile for $T_{db} = 283$ K and $\psi = 10\%$. The droplet temperature eventually reaches an equilibrium (wet-bulb temperature, T_{wb}) after a transient period, due to the previously described mechanism. Panel (b) of the same figure presents the temperature field at this equilibrium condition. We also conducted simulations for various combinations of T_{db} and ψ, comparing the resulting equilibrium droplet temperatures to the expected wet-bulb temperature (T_{wb}) derived from psychrometric data. Fig. 5 displays the numerical results of the wet-bulb temperature in comparison to psychrometric data for several ψ and T_{db} combinations on the finest grid considered (256×256). The numerical results show a strong agreement with the psychrometric data, validating the method accuracy in replicating the expected physical behavior.

4.1.3. Evaporating droplet falling under gravity in a confining container

Next we consider a droplet undergoing evaporation when subjected to significant deformations, thermal gradients, and in presence of solid boundaries. The setup involves a droplet with an initial diameter d_0 descending within a heated, vertically aligned container under gravitational forces, acting in the negative y-direction. The droplet is positioned at the top of the container of dimensions $[0, 4d_0] \times [0, 16d_0]$. The experiment enforces no-slip and no-penetration conditions (wall) at all container boundaries, with the exception of the top, where fluid is allowed to exit under a zero-pressure condition. The temperature at the walls (T_w) is controlled using Dirichlet boundary conditions, setting a higher temperature than the initial uniform temperature ($T_0 = 0.8 T_{sat} < T_w$), with (zero) Neumann boundary condition is applied at the outflow. Similarly, zero-Dirichlet boundary conditions are imposed for the vapor mass fraction (hence, $\xi_w = 0$) at the walls, with a zero-flux condition at the outflow. The mass fraction field is initialized as previously described. The relevant flow parameters are summarized in Table 3.

Fig. 6 shows the contour plots of the temperature at different time instants during the life of the droplet, as it falls due to gravity. For this case, the Schmidt number and density ratio are chosen to be $Sc = 0.1$ and $r_\rho = 10$, respectively. Initially, the temperature is larger near the walls because $T_w > T_0$. Over time, however, heat conduction diminishes the temperature gradients within the gaseous phase. Additionally, the reduced gas temperature near the droplet interface is clearly observable, which is explained by the evaporative cooling effect. The grid convergence of the solution for this more complex case is illustrated in Fig. 7. These results are also compared with those obtained using a different solver available in our group, which simulates droplet evaporation based on the Volume-of-Fluid method (for more details, see [30] and [25,82]). The results once again confirm the accuracy and validity of the proposed model. It is worth mentioning that using the Conservative Diffuse Interface (CDI) approach requires double the resolution to converge to the results obtained with the VOF method, as seen in Fig. 7. This requirement arises from the thicker interface associated with the CDI method, a limitation also demonstrated by [84] in the absence of phase change. However, this

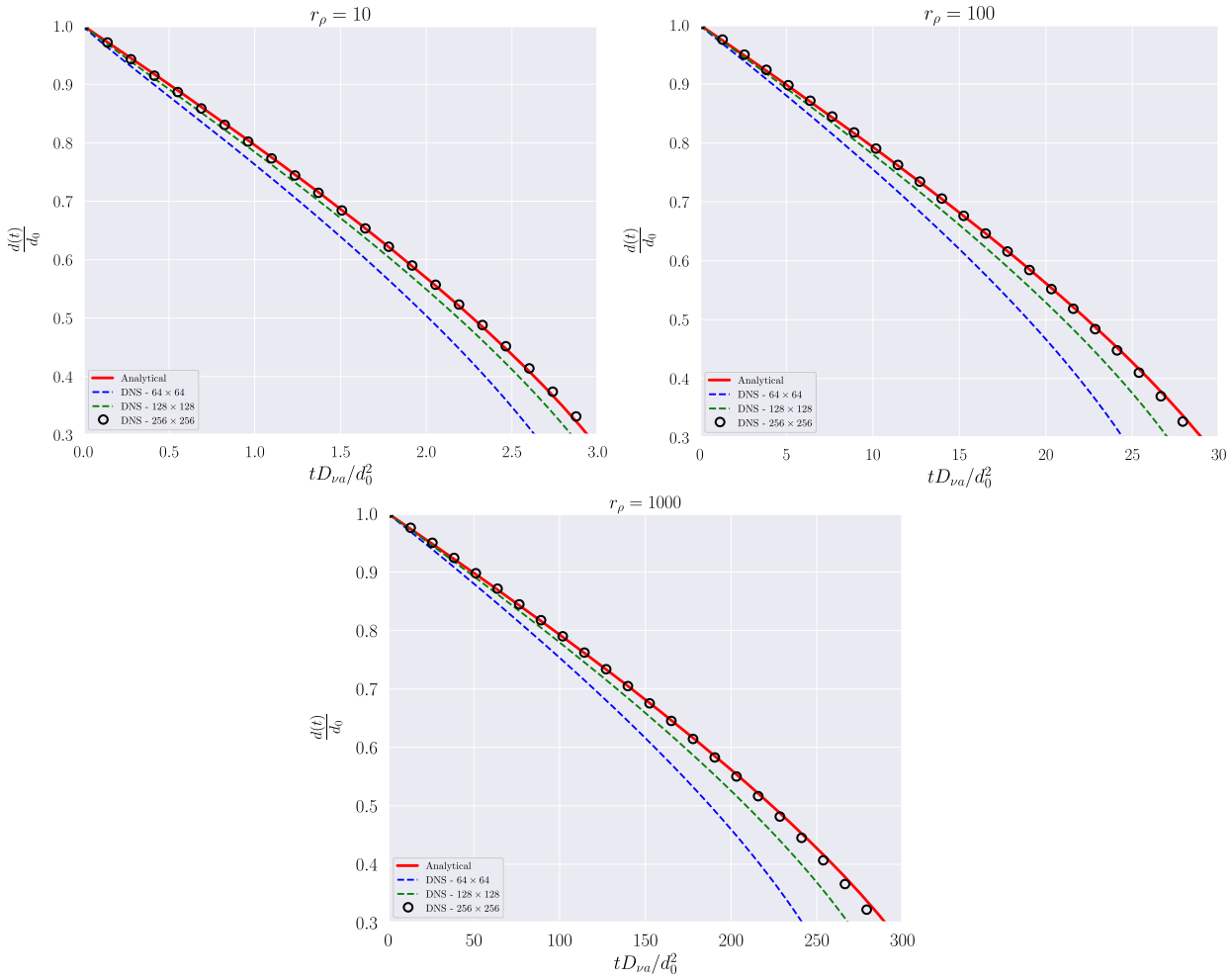

Fig. 2. Time history of the normalized droplet diameter for varying density ratios (r_ρ) illustrated alongside results from grid convergence tests.

limitation can be mitigated by employing the Accurate Conservative Diffuse Interface (ACDI) method, as shown in Ref. [100]. The ACDI method achieves comparable accuracy to CDI while requiring only half the resolution, primarily due to its sharper interface.

Finally, two additional simulations were conducted with higher density ratios of 100 and 1000, and the temporal evolution of droplet volume for these cases is shown in Fig. 8. Since the evaporation rate decreases significantly with increasing density ratio, a higher vapor diffusivity coefficient ($Sc = 0.001$) was chosen to enhance evaporation. These results further demonstrate the robustness of the proposed numerical model in accurately simulating complex scenarios involving high density ratios and phase change within a dynamic environment.

4.2. Incompressible liquid phase & compressible gas phase

In this section, we treat the liquid as incompressible, assuming constant and uniform thermophysical properties. Conversely, the gas is considered compressible, with properties that vary as a function of temperature, thermodynamic pressure, and composition. Given the potential variations in density, we account for compressibility within the low-Mach limit. This approach enables filtering acoustic waves while preserving density variations in the bulk region of the gas phase. For this purpose, we solve the set of equations (61).

4.2.1. Static droplet evaporating in two-dimensional open domain

In this test case, we consider a stationary two-dimensional circular droplet and impose zero-pressure outflow boundary conditions, hence $p_0 = p_0(t = 0)$. The enthalpy equation is solved with Dirichlet boundary conditions at all boundaries with uniform temperature initialized as $T_0 = 0.8\,T^{sat}$. As in the previous cases, the steady state solution of eq. (61c) with $\vec{u} = 0$ is used as initial condition for ξ, with Dirichlet boundary conditions at the domain boundaries.

The governing equations are solved within a square domain $[-2d_0, 2d_0]^2$ using 256×256 grid points. This scenario has been replicated using the Volume-of-Fluid solver developed by our group for simulating droplet evaporation in the low-Mach number limit (for further details, see [82]). The comparison of the temporal evolution of droplet volume between the two models demonstrates a

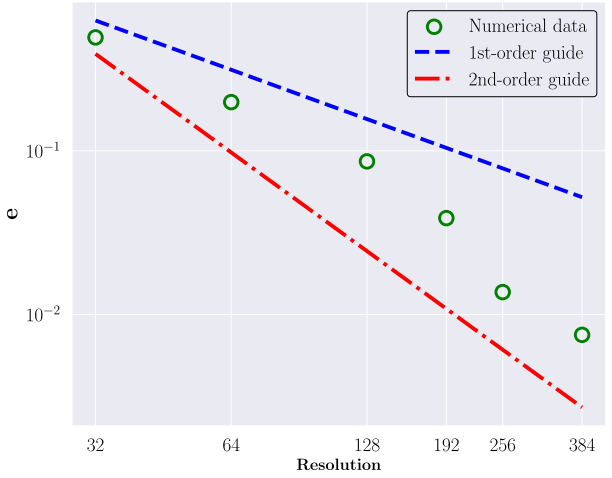

Fig. 3. Error in normalized droplet mass, $M/M_{t=0}$, for $r_\rho = 1000$ and $d(t)/d_0 = 0.5$.

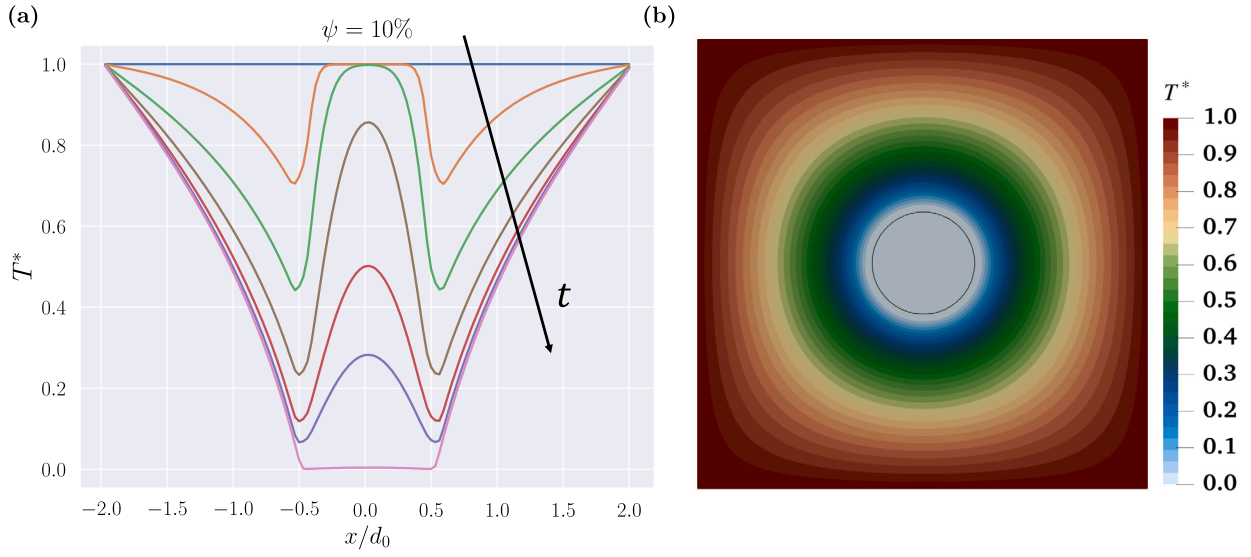

Fig. 4. Evaporating static droplet with $T_{db} = 283$ K and $\psi = 10\%$. (a): Time evolution of the normalized temperature profile $T^* = (T - T_{wb,0})/(T_\infty - T_{wb,0})$ along $x = 0$ at $tD_{vg}/d_0^2 = \{0, 0.95, 3.8, 22.8, 34.2, 45.6, 142.7\}$. (b): Contours of normalized temperature at $t = 178.4\, d_0^2/D_{va}$.

good agreement, as illustrated in Fig. 9(a). Fig. 9(b) displays one-dimensional profiles showing variations in gas density, temperature, and liquid volume fraction along the center-line. We can observe that the droplet volume decreases due to evaporation (i.e., the area delimited by α_1 has shrunk), and the temperature near the interface is lower due to the evaporative cooling effect. Consequently, the density of the gas phase locally increases. It is worth noting that the boundedness of α_1 has been maintained throughout the simulation, as evident in Fig. 9(b). Note also that the same resolution is adopted with the two approaches, VoF and PF, giving similar results as long as the resolution is adequate.

4.2.2. Droplet sedimenting in three-dimensional domain

This section outlines the simulation of a single droplet that sediments, deforms, and evaporates in a non-isothermal environment. We consider an initially spherical droplet with diameter d_0, positioned in the domain $[0, 5d_0] \times [0, 5d_0] \times [0, 10d_0]$, with gravity acting in the negative vertical direction. The droplet starts at rest, centered at the top of the domain, at coordinates $[2.5, 2.5, 8]d_0$. The domain has periodic boundaries in all directions and is discretized with $320 \times 320 \times 640$ grid cells. The initial temperature is uniformly set to $0.95T_{\text{sat}}$, and the mass fraction field is initialized with the steady-state solution of the governing equation considering $\vec{u} = 0$. The relevant parameters are summarized in Table 3. Unlike the previous case, because of the periodic boundary conditions, the thermodynamic pressure within the domain varies over time following eq. (42), and the vaporized liquid is confined within the domain, as shown in Fig. 10. The time history of the droplet volume is depicted in Fig. 11.

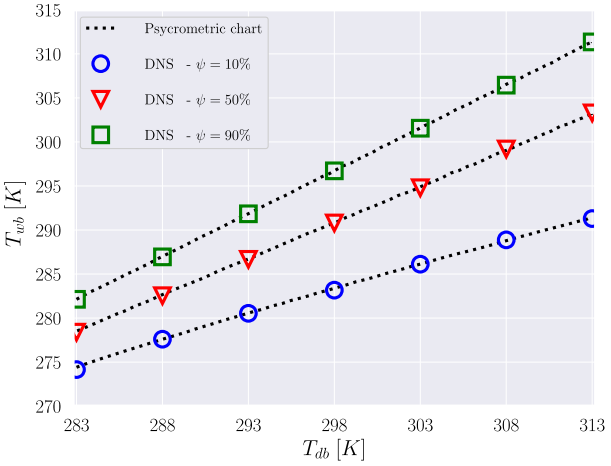

Fig. 5. Numerical results of the wet bulb temperature (T_{wb}) for an evaporating static droplet, compared with psychrometric chart values, varying dry bulb temperature (T_{db}) and relative humidity (ψ), on a 256×256 grid.

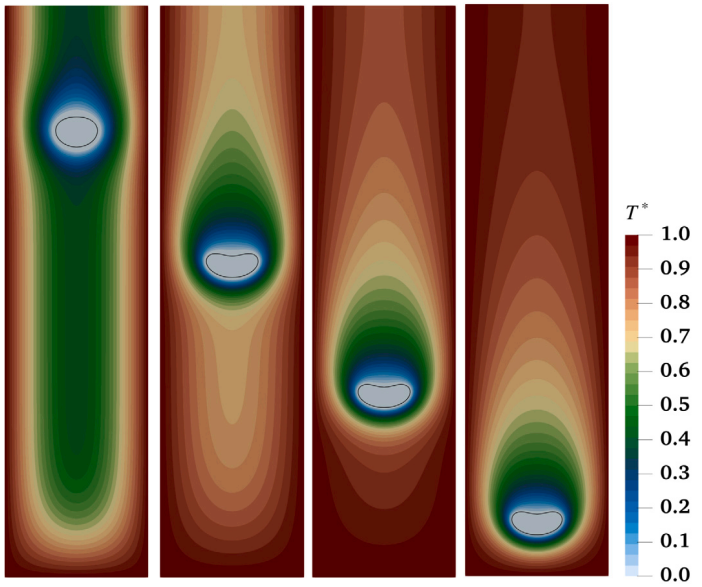

Fig. 6. Evaporation of a two-dimensional sedimenting droplet on a 512×2048 grid. Contour plots of normalized temperature ($T^* = (T - T_0)/(T_w - T_0)$) at four time-instants (from left to right): $t\sqrt{|\vec{g}|/d_0} = 2.55, 5.10, 7.66$ and 10.21. The solid black line represents the interface at $\alpha_1 = 0.5$.

The simulations presented here show the potential of the model to handle evaporation in suspensions of deformable droplets while exactly conserving the mass of the different species. As shown above, the algorithm is suitable for high-density ratio and a more complex thermodynamic description, within the low Mach limit. Future studies will consider several droplet and how their hydrodynamic interactions may alter the total evaporation rate.

5. Conclusion

This study presents a novel diffuse-interface model designed for simulating low Mach number multicomponent two-phase flows with phase change. The model system is derived in the low Mach number limit from the four-equation two-phase model that is obtained from the general seven-equation Baer-Nunziato model by assuming instantaneous kinetic, mechanical and thermal equilibrium. A multicomponent extension of the model is introduced to describe flows where the gaseous component is made of vapor and inert gas. The model includes a mass transfer term whose formulation is obtained by considering phase change driven by the difference of chemical potentials of the phases. Additionally, a simplified model has been introduced for a fully incompressible system with mass transfer and phase transition.

The general numerical strategy is detailed in Section 3, and the pseudo-algorithm, along with an extensive description of the spatial discretization, is presented in Appendix D. Central difference schemes have been used for all spatial operators in the model. This leads

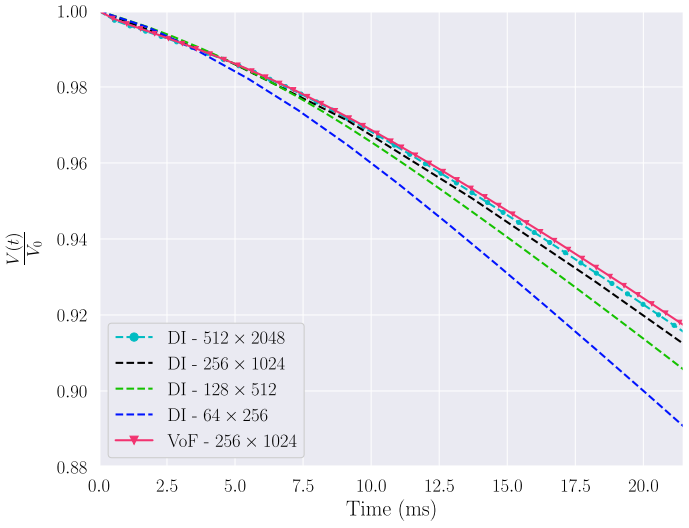

Fig. 7. Grid convergence study for a sedimenting droplet with $r_\rho = 10$ and $Sc = 0.1$, illustrating the temporal evolution of the droplet volume and comparing the results to a sharp-interface model with a resolution of 256×1024.

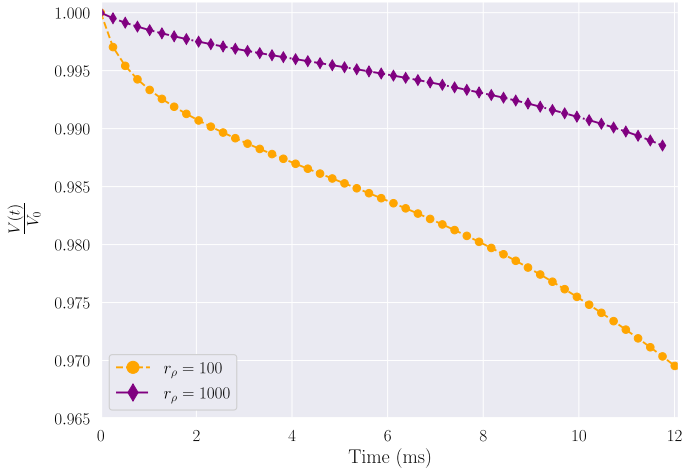

Fig. 8. Temporal evolution of a sedimenting droplet's volume for cases with high density ratios (100 and 1000), computed at a resolution of 256×1024 and $Sc = 0.001$.

to a non-dissipative discrete implementation, crucial for accurately simulating turbulent flows. Interface-regularization terms have been employed to maintain the interface thickness throughout the simulations and prevent artificial diffusion of the interface. The proposed method conserves at the discrete level the mass of each phase, the momentum and enthalpy of the system.

In this study, we opted for the diffuse interface approach rather than a sharp-interface formulation. The diffuse interface approach effectively captures the interface without requiring dedicated boundary conditions. These methods are based on thermodynamic principles, allowing for the incorporation of different physical effects through adjustments to the free energy. While the diffuse interface approach uses an interface thickness that is significantly larger than the physical thickness, it ensures thermodynamic consistency across the entire domain. Furthermore, it supports the natural dynamic creation and disappearance of interfaces, which is essential for accurately simulating processes such as boiling and evaporation.

We conducted extensive numerical simulations and tests using our model to assess and validate the newly introduced diffuse-interface methodology with phase transition. For a fully incompressible system, this included: (a) validating against the available analytical solution for isothermal evaporation; (b) validating against experimental data from a psychrometric chart for thermal evaporation under various thermodynamic conditions; and (c) comparing the diffuse-interface results with those from the sharp-interface approach in the case of a sedimenting droplet in a confined container. For the system with compressible gas phase, our tests included: (d) examining a static droplet evaporating in an open domain and comparing the results of the diffuse-interface approach with those from the sharp-interface method; and (e) conducting a three-dimensional simulation of a sedimenting droplet in a closed domain, where the droplet evaporates, deforms, and thermodynamic pressure varies.

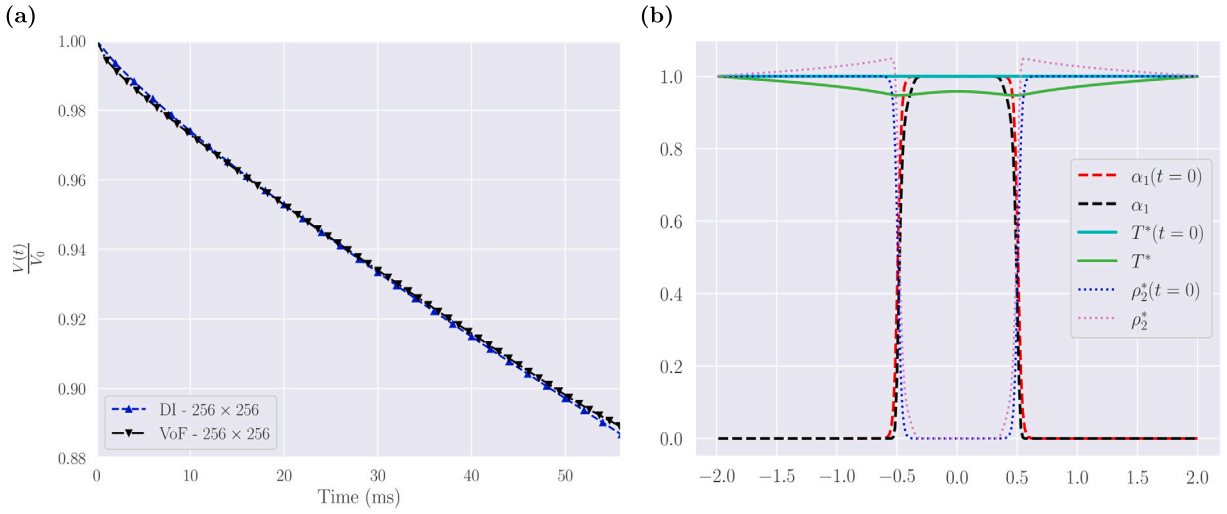

Fig. 9. (a) Predicted temporal evolution of instantaneous droplet volume over the initial value (V/V_0) shown in comparison to the result of the sharp-interface model. (b) One-dimensional profiles of liquid volume fraction (α_1), normalized temperature ($T^* = T/T(t=0)$) and normalize gas-phase density ($\rho_2^* = \rho_2/\rho_2(t=0)$) at the initial time and at $t = 40(ms)$.

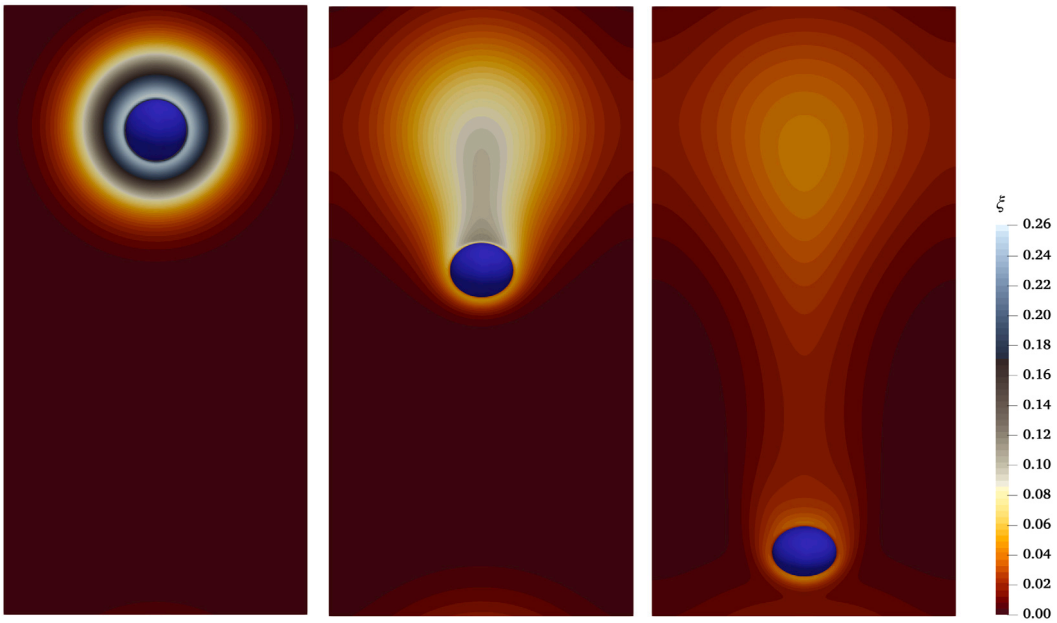

Fig. 10. Contours of vapor mass fraction (ξ) in the $y = 2.5d_0$ plane at time instants t [ms] = 6, 36, and 66.

In the future, we plan to extend the numerical code to handle wetting and contact-line boundary condition, following the approach for the fully-compressible boiling in [85]. Note also that the formulation presented here can also be directly extended to consider multicomponent mixtures, see as example [29,30] for a similar implementation with a sharp-interface tracking.

CRediT authorship contribution statement

Salar Zamani Salimi: Writing – original draft, Visualization, Validation, Software, Methodology, Investigation, Formal analysis, Conceptualization. **Aritra Mukherjee:** Writing – review & editing, Software, Methodology, Investigation, Conceptualization. **Marica Pelanti:** Writing – review & editing, Writing – original draft, Methodology, Formal analysis, Conceptualization. **Luca Brandt:** Writing – review & editing, Supervision, Resources, Methodology, Conceptualization.

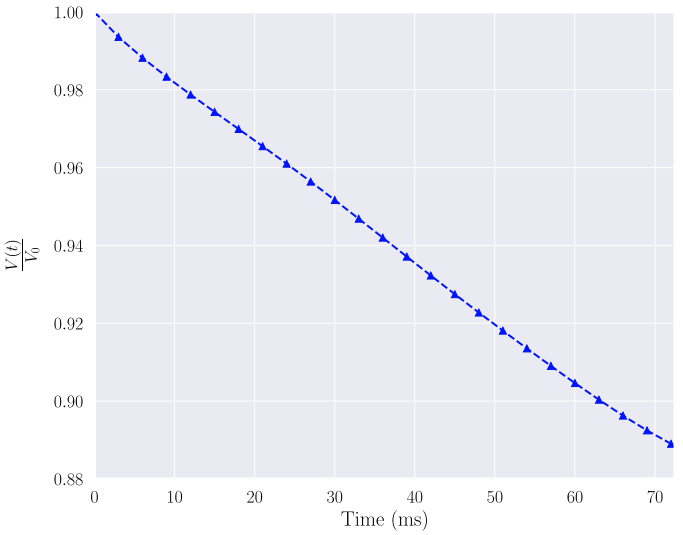

Fig. 11. Temporal evolution of the normalized droplet volume (V/V_0) using a resolution of $320 \times 320 \times 640$.

Declaration of competing interest

The authors declare that they have no known competing financial interests or personal relationships that could have appeared to influence the work reported in this paper.

Appendix A. Derivation of the expression of $\vec{\nabla} \cdot \vec{u}$ for the multicomponent model

In this section we show the derivation of the equation for $\vec{\nabla} \cdot \vec{u}$ written in (37)-(38) for the multicomponent liquid-vapor-gas model presented in Section 2.3 (system (39)). We start by writing

$$\vec{\nabla} \cdot \vec{u} = -\frac{1}{\rho}\frac{D\rho}{Dt} = \frac{1}{v}\frac{Dv}{Dt}, \tag{A.1}$$

where $\frac{D}{Dt} = \frac{\partial}{\partial t} + \vec{u} \cdot \vec{\nabla}$, and $v = 1/\rho$. We have

$$v = Y_1 v_1 + (1 - Y_1) v_2, \quad Y_1 = \frac{\alpha_1 \rho_1}{\rho}, \quad v_1 = \frac{1}{\rho_1} = \text{const.}, \quad v_2 = \frac{1}{\rho_2}, \quad \rho_2 = \frac{p M_2(\xi)}{\mathcal{R} T} = \rho_2(p, T, \xi). \tag{A.2}$$

Therefore

$$\frac{Dv}{Dt} = (v_1 - v_2)\frac{DY_1}{Dt} + Y_2 \left(\frac{\partial v_2}{\partial p}\Big|_{T,\xi} \frac{dp_0}{dt} + \frac{\partial v_2}{\partial T}\Big|_{p,\xi} \frac{DT}{Dt} + \frac{\partial v_2}{\partial \xi}\Big|_{p,T} \frac{D\xi}{Dt} \right). \tag{A.3}$$

Because the equation for the mass fraction $Y_1 = \frac{\alpha_1 \rho_1}{\rho}$ is

$$\partial_t Y_1 + \vec{u} \cdot \vec{\nabla} Y_1 = \frac{\mathcal{M}}{\rho}, \tag{A.4}$$

we obtain:

$$\vec{\nabla} \cdot \vec{u} = \left(\frac{1}{\rho_1} - \frac{1}{\rho_2} \right) \mathcal{M} + \alpha_2 \left[-\frac{1}{p_0}\frac{dp_0}{dt} + \frac{1}{T}\frac{DT}{Dt} + M_2(\xi) \left(\frac{1}{M_v} - \frac{1}{M_a} \right) \frac{D\xi}{Dt} \right]. \tag{A.5}$$

By using now the equation for the mass fraction ξ,

$$\partial_t \xi + \vec{u} \cdot \vec{\nabla} \xi = -\frac{1 - \xi}{\alpha_2 \rho_2} \mathcal{M} + \frac{1}{\alpha_2 \rho_2} \vec{\nabla} \cdot (\alpha_2 \rho_2 D_{va} \vec{\nabla} \xi), \tag{A.6}$$

we have

$$\begin{aligned} \vec{\nabla} \cdot \vec{u} = & \left[\left(\frac{1}{\rho_1} - \frac{1}{\rho_2} \right) - (1 - \xi) \frac{M_2(\xi)}{\rho_2} \left(\frac{1}{M_v} - \frac{1}{M_a} \right) \right] \mathcal{M} \\ & - \frac{\alpha_2}{p_0}\frac{dp_0}{dt} + \frac{\alpha_2}{T}\frac{DT}{Dt} + \frac{M_2(\xi)}{\rho_2} \left(\frac{1}{M_v} - \frac{1}{M_a} \right) \vec{\nabla} \cdot (\alpha_2 \rho_2 D_{va} \vec{\nabla} \xi). \end{aligned} \tag{A.7}$$

The equation for the specific enthalpy h reduces to

$$\partial_t h + \vec{u}\cdot\vec{\nabla}h = \frac{1}{\rho}\vec{\nabla}\cdot(\lambda_c\vec{\nabla}T) + \frac{\alpha_2}{\rho}\frac{dp_0(t)}{dt}. \tag{A.8}$$

Recalling that $h = Y_1h_1 + Y_2h_2 = Y_1h_1 + Y_2(\xi h_v + (1-\xi)h_a) = h(Y_1,\xi,T)$, we obtain the equation for T:

$$\partial_t T + \vec{u}\cdot\vec{\nabla}T = \frac{1}{\rho(Y_1\kappa_{p1} + Y_2\kappa_{p2}(\xi))}\left[\vec{\nabla}\cdot(\lambda_c\vec{\nabla}T) + \alpha_2\frac{dp_0(t)}{dt} + (h_v - h_1)\mathcal{M} + (h_a - h_v)\mathcal{D}\right], \tag{A.9}$$

where we have denoted as before $\mathcal{D} = \vec{\nabla}\cdot(\alpha_2\rho_2 D_{va}\vec{\nabla}\xi)$. Let us observe that the mass transfer term multiplied by the latent heat $L_{\text{lat}} = (h_v - h_1)$ appears in the temperature equation (while there is no mass transfer contribution in the equation for the mixture enthalpy, as also noted in [94]). Finally the divergence constraint for $\vec{\nabla}\cdot\vec{u}$ has the expression reported in (37):

$$\vec{\nabla}\cdot\vec{u} = \bar{Z}\mathcal{M} + \bar{B}\vec{\nabla}\cdot(\lambda_c\vec{\nabla}T) + \bar{D}\mathcal{D} - \bar{K}_S\frac{dp_0(t)}{dt}, \tag{A.10}$$

where the mixture quantities $\bar{K}_S$, $\bar{B}$, $\bar{Z}$, $\bar{D}$ are defined in (38a), (38b), (38c), (38d).

Appendix B. Consistency of the expression for the velocity divergence, $\vec{\nabla}\cdot\vec{u}$

In this section we show that the equation for $\vec{\nabla}\cdot\vec{u}$ (37), (39e) derived in Appendix A from the equation for the total density ρ (see equation (A.1)) by using the mass fraction and enthalpy equations is consistent with the equation for $\vec{\nabla}\cdot\vec{u}$ (22d) in the low-Mach number model with general equations of state, when a single-component gas made of vapor is considered, $\xi = 1$. More specifically, we wish to show that for an incompressible phase 1 and for $\xi = 1$ we have

$$\bar{K}_s = \frac{1}{\rho c^2}, \quad \bar{B} = \frac{S_p^e}{\rho c^2}, \quad \bar{Z} = \frac{S_p}{\rho c^2}, \tag{B.1}$$

where c, S_p^e, S_p are given in (2), (6), (5), respectively, and $\bar{K}_s$, $\bar{B}$, $\bar{Z}$ in (38d), (38c), (38a). The first relation above shows that $\bar{K}_s$ correctly represents the mixture compressibility in the diffuse interface zone. First, we observe that for the incompressible liquid we have:

$$K_{s1} = \frac{1}{\rho_1 c_1^2} = 0, \quad \beta_1 = \frac{\Gamma_1\kappa_{p1}}{c_1^2} = 0 \Rightarrow B_1 \equiv \frac{\Gamma_1}{\rho_1 c_1^2} = 0, \quad \phi_1 = 0, \quad \zeta_1 = 0. \tag{B.2}$$

Phase 2 is an ideal gas, hence we have (considering $p = p_0$)

$$K_{s2} = \frac{1}{\rho_2 c_2^2} = \frac{1}{\gamma_2 p_0}, \quad \beta_2 = \frac{1}{T}, \quad \phi_2 = -\frac{\rho_2}{T}, \quad \zeta_2 = \frac{\rho_2}{p_0}. \tag{B.3}$$

By using (B.2) equation (2) gives:

$$\frac{1}{\rho c^2} = \frac{\alpha_2}{\rho_2 c_2^2} + \frac{TC_{p1}C_{p2}}{C_{p1}+C_{p2}}\left(\frac{\Gamma_2}{\rho_2 c_2^2}\right)^2. \tag{B.4}$$

By using then the relations $\frac{1}{\rho_2 c_2^2} = \frac{1}{\gamma_2 p_0} = \frac{1}{p_0} - \frac{\gamma_2 - 1}{\gamma_2 p_0} = \frac{1}{p_0} - \frac{1}{T\rho_2\kappa_{p2}}$ and $\frac{\Gamma_2}{\rho_2 c_2^2} = \frac{1}{T\rho_2\kappa_{p2}}$, we can write

$$\frac{1}{\rho c^2} = \frac{\alpha_2}{p_0} - \frac{\alpha_2}{T\rho_2\kappa_{p2}} + + \frac{T\alpha_1\rho_1\kappa_{p1}\alpha_2\rho_2\kappa_{p2}}{\alpha_1\rho_1\kappa_{p1} + \alpha_2\rho_2\kappa_{p2}}\frac{1}{(T\rho_2\kappa_{p2})^2} = \frac{\alpha_2}{p_0} - \frac{\alpha_2^2}{T(\alpha_1\rho_1\kappa_{p1} + \alpha_2\rho_2\kappa_{p2})}, \tag{B.5}$$

which agrees with (38d). Now we consider S_p^e in (6). The numerator reduces to $\alpha_2\phi_2\rho_1 = -\frac{\alpha_2}{T}\rho_2\rho_1$, based on (B.2) and (B.3). By observing, based on (9), that $\frac{\rho_1 c_1^2}{\Gamma_1}\phi_1 = -\rho_1^2\kappa_{p1}$ and $\frac{\rho_1 c_1^2}{\Gamma_1}\zeta_1 = 0$, the denominator D_T becomes:

$$D_T = -\alpha_1\alpha_2\kappa_{p1}\zeta_2\rho_1^2 + \alpha_2^2\frac{\phi_2\rho_1}{\Gamma_2} = -\alpha_1\alpha_2\kappa_{p1}\rho_1^2\frac{\rho_2}{p_0} - \alpha_2^2\frac{\rho_1\rho_2^2\kappa_{p2}}{p_0\gamma_2}, \tag{B.6}$$

where we have used the relations in (B.3) and $\frac{\rho_2}{T\Gamma_2} = \frac{\rho_2^2\kappa_{p2}}{\gamma_2}$. We then easily see that by using the above expressions we obtain:

$$\frac{1}{D_T\rho c^2} = -\frac{1}{(\alpha_1\rho_1\kappa_{p1} + \alpha_2\rho_2\kappa_{p2})\rho_1\rho_2}. \tag{B.7}$$

Hence we finally obtain

$$\frac{S_p^e}{\rho c^2} = \frac{\alpha_2}{T(\alpha_1\rho_1\kappa_{p1} + \alpha_2\rho_2\kappa_{p2})}, \tag{B.8}$$

which agrees with $\bar{B}$ in (38c).

Finally we consider S_p in (5), which we can rewrite as (see also Appendix B of [98]):

$$S_p = \frac{1}{D_T}\left[\left(\alpha_1\frac{\chi_1}{\Gamma_1}\phi_1 + \alpha_2\frac{\chi_2}{\Gamma_2}\phi_2\right)(\rho_2-\rho_1) + (\rho_2 h_2 - \rho_1 h_1)(\alpha_1\phi_1 + \alpha_2\phi_2)\right]. \tag{B.9}$$

By using (B.2), (B.3), and the relations $\chi_2 = 0$, $\frac{\chi_1}{\Gamma_1}\phi_1 = -\rho_1\kappa_{p1}$, $h_2 = \kappa_{p2}T$, the numerator can be written as:

$$-(\alpha_1\rho_1\kappa_{p1} + \alpha_2\rho_2\kappa_{p2})(\rho_2-\rho_1) - \frac{\alpha_2\rho_1\rho_2}{T}(h_2-h_1). \tag{B.10}$$

Using the result in (B.7) we obtain

$$\frac{S_p}{\rho c^2} = \frac{\rho_2-\rho_1}{\rho_1\rho_2} + \frac{\alpha_2(h_2-h_1)}{T(\alpha_1\rho_1\kappa_{p1} + \alpha_2\rho_2\kappa_{p2})}, \tag{B.11}$$

which agrees with $\bar{Z}$ in (38a) for $\xi = 1$ (which implies $h_2 = h_v$). Let us also observe that the average quantities $\bar{K}_s$ and $\bar{B}$ recover the correct limit for pure liquid ($\alpha_2 = 0$), for which we have $\vec{\nabla}\cdot\vec{u} = 0$. Indeed for $\alpha_k = 0$ we have, based on the relations (B.1), $\bar{B} = \frac{\Gamma_k}{\rho_k c_k^2} = \frac{\beta_k}{\rho_k\kappa_{pk}}$ and $\bar{K}_S = K_{Sk} = \frac{1}{\rho_k c_k^2}$, and for the liquid $K_{S1} = \beta_1 = 0$.

Appendix C. Boiling flow model

Although the main focus of this work is on evaporation processes, the low Mach number model derived in Section 2.2 can be used to describe boiling flows as well. For boiling phenomena we can consider a two-phase flow made of weakly compressible liquid and vapor phases governed by equations (22) (that we repeat here for clarity):

$$\partial_t(\alpha_1\rho_1) + \vec{\nabla}\cdot(\alpha_1\rho_1\vec{u}) = \mathcal{M}, \tag{C.1a}$$

$$\partial_t(\alpha_2\rho_2) + \vec{\nabla}\cdot(\alpha_2\rho_2\vec{u}) = -\mathcal{M}, \tag{C.1b}$$

$$\partial_t(\rho\vec{u}) + \vec{\nabla}\cdot(\rho\vec{u}\otimes\vec{u}) + \vec{\nabla}\tilde{p} = \vec{\nabla}\cdot\vec{\tau} + \vec{\Sigma} + \rho\vec{\mathfrak{g}}, \tag{C.1c}$$

$$\vec{\nabla}\cdot\vec{u} = \frac{S_p}{\rho c^2(Y_1,h,p_0)}\mathcal{M} + \frac{S_p^e}{\rho c^2(Y_1,h,p_0)}\vec{\nabla}\cdot(\lambda_c\vec{\nabla}T) - \frac{1}{\rho c^2(Y_1,h,p_0)}\frac{dp_0(t)}{dt}, \tag{C.1d}$$

$$\partial_t(\rho h) + \vec{\nabla}\cdot(\rho h\vec{u}) = \vec{\nabla}\cdot(\lambda_c\vec{\nabla}T) + \frac{dp_0(t)}{dt}. \tag{C.1e}$$

The mass transfer term can be defined as in (43) as a relaxation term that depends on the difference of the liquid and vapor chemical potentials μ_k^p, $k = 1,2$. Here, we write a variant of the expression in (43) that vanishes automatically in regions of pure liquid or pure vapor:

$$\mathcal{M} = \frac{1}{\Omega_\mu\tau}\cdot\frac{\alpha_1\rho_1\alpha_2\rho_2}{\alpha_1\rho_1 + \alpha_2\rho_2}(\mu_2^p - \mu_1^p). \tag{C.2}$$

Since both liquid and vapor are assumed pure constituents, their chemical potential is equal to their free Gibbs energy: $\mu_k^p(p,T) = g_k(p,T)$. Different choices can be made for the equations of state of the phases, of varying accuracy and complexity. In [75], we adopted for instance the Noble–Able Stiffened Gas (NASG) equation of state for each phase [109]. This is a relatively simple EOS, which nonetheless provides a more accurate model than the incompressible liquid and ideal gas model of Section 2.3. The NASG EOS for phase k has the form:

$$p_k(\mathcal{E}_k,\rho_k) = \frac{\gamma_k-1}{1-\rho_k b_k}(\mathcal{E}_k - \eta_k\rho_k) - \gamma_k\varpi_k, \tag{C.3a}$$

$$T_k(p_k,\rho_k) = \frac{(1-\rho_k b_k)(p_k+\varpi_k)}{\kappa_{vk}\rho_k(\gamma_k-1)}. \tag{C.3b}$$

Here γ_k, ϖ_k, η_k, b_k, κ_{vk} are material-dependent constant parameters. The specific entropy s_k, the specific enthalpy h_k, and the specific Gibbs free energy are (setting here $p_1 = p_2 = p$ and $T_1 = T_2 = T$)

$$s_k(p,T) = \kappa_{vk}\log\frac{T^{\gamma_k}}{(p+\varpi_k)^{\gamma_k-1}} + \tilde{\eta}_k, \tag{C.4a}$$

$$h_k(T,p) = \kappa_{pk}T + b_k p + \eta_k, \tag{C.4b}$$

$$g_k(p,T) = (\gamma_k\kappa_{vk} - \tilde{\eta}_k)T - \kappa_{vk}T\log\frac{T^{\gamma_k}}{(p+\varpi_k)^{\gamma_k-1}} + \eta_k + b_k p, \tag{C.4c}$$

where $\kappa_{pk} = \gamma_k\kappa_{vk}$ (specific heat capacity at constant pressure) and $\tilde{\eta}_k$ are constant parameters. Given the NASG equations of state for the liquid and vapor phases of a species the theoretical pressure-temperature saturation curve is determined by the chemical potential equilibrium condition $g_1(p,T) = g_2(p,T)$. This gives the following p-T saturation curve:

$$A_s + \frac{B_s}{T} + C_s \log T + D_s \log(p + \varpi_1) - \log(p + \varpi_2) + \frac{p\, E_s}{T} = 0, \tag{C.5}$$

where

$$A_s = \frac{\kappa_{p1} - \kappa_{p2} - \tilde{\eta}_1 + \tilde{\eta}_2}{\kappa_{p2} - \kappa_{v2}},\ B_s = \frac{\eta_1 - \eta_2}{\kappa_{p2} - \kappa_{v2}},\ C_s = \frac{\kappa_{p2} - \kappa_{p1}}{\kappa_{p2} - \kappa_{v2}},\ D_s = \frac{\kappa_{p1} - \kappa_{v1}}{\kappa_{p2} - \kappa_{v2}},\ E_s = \frac{b_1 - b_2}{\kappa_{p2} - \kappa_{v2}}. \tag{C.6}$$

The constant parameters in the NASG equations of state of the two phases are determined so that the associated theoretical saturation curves match the experimental saturation curves for the considered material, at least in a certain temperature range, see [109].

Appendix D. Pseudo-algorithm

For simplicity, we focus on a 2D configuration. The detailed pseudo-algorithm for the coupled two-phase solver with phase transition is provided below. To simplify and emphasize the spatial discretizations, the pseudo-algorithm is presented using first-order explicit Euler time integration. Extending it to higher-order time-stepping schemes is straightforward. To simplify the notation, we denote the velocity components in the x and y directions as u and v, respectively. Therefore, the x-component of velocity on the left face of the cell at position (i, j) is denoted as $u_{i-1/2,j}$. The mass fluxes are represented similarly, with U and V indicating the mass fluxes in the x and y directions. The governing equations are advanced in time by $\Delta t^{k+1} = t^{k+1} - t^k$, with the previous time-step indicated with $\Delta t^k = t^k - t^{k-1}$. In this section, eqs. (61) are the target governing equations derived for a system where the liquid phase is treated as incompressible and the gas phase is considered compressible under the low-Mach number limit, resulting in varying thermophysical properties of the gas phase. It is also worth mentioning that there are two strategies available for updating the thermodynamic pressure at the new timestep: one involves using the expression for $\frac{dp_0(t)}{dt}$ as shown in eq. (42) and advancing the thermodynamic pressure (p_0) based on the Adam-Bashforth time integration scheme; the other involves using the ideal gas equation of state as in eq. (30). We have chosen to use the ideal gas equation of state (30), following Dalla Barba et al. [110], to ensure mass conservation for the compressible gas phase at a discrete level. Accordingly, p_0^{k+1} is calculated by integrating the gas density over the total volume of the gas phase, $p_0^{k+1} = \dfrac{M_g^{k+1}}{\displaystyle\int_{V_g^{k+1}} \frac{M_2^{k+1}}{\mathcal{R} T^{k+1}}\, dV_g^{k+1}}$, where M_g and V_g denote the total mass and the entire volume of the gas phase. The reduction of the following algorithm to a fully incompressible system is straightforward. Below to simplify the notation we will denote with p the hydrodynamic pressure, which was indicated with $\tilde{p}$ in the system (61).

1. Compute the gas-phase thermophysical properties at the cell centers:
   - $\lambda_{2\,i,j}^k = (1 - \xi_{i,j}^k)\, \lambda_a + \xi_{i,j}^k\, \lambda_v$
   - $\kappa_{p2\,i,j}^k = (1 - \xi_{i,j}^k)\, \kappa_{pa} + \xi_{i,j}^k\, \kappa_{pv}$
   - $M_{2\,i,j}^k = \Big(\dfrac{(1 - \xi_{i,j}^k)}{M_a} + \dfrac{\xi_{i,j}^k}{M_v}\Big)^{-1}$
   - $\rho_{2\,i,j}^k = \dfrac{p_0^k M_{2\,i,j}^k}{\mathcal{R} T_{i,j}^k}$
2. Compute mixture thermophysical properties at the cell centers:
   - $\lambda_{i,j}^k = \alpha_{2\,i,j}^k\, \lambda_{2\,i,j}^k + \alpha_{1\,i,j}^k\, \lambda_1$
   - $\kappa_{p\,i,j}^k = \alpha_{2\,i,j}^k\, \kappa_{p2\,i,j}^k + \alpha_{1\,i,j}^k\, \kappa_{p1}^k$
   - $\rho_{i,j}^k = (\alpha_2\, \rho_2)_{i,j}^k + \alpha_{1\,i,j}^k\, \rho_1$
   - $(\rho\kappa_p)_{i,j}^k = (\alpha_2\, \rho_2)_{i,j}^k \kappa_{p2\,i,j}^k + \alpha_{1\,i,j}^k\, \rho_1\, \kappa_{p1}$
   - $\mu_{i,j}^k = \alpha_{2\,i,j}^k\, \mu_2 + \alpha_{1\,i,j}^k\, \mu_1$
3. Compute body forces (including surface tension force):
   - Compute normal vectors at the cell centers:
     - Compute $\nabla\alpha_1$ at cell centers: $\nabla\alpha_{1\,i,j}^k = \Big(\dfrac{\alpha_{1\,i+1,j}^k - \alpha_{1\,i-1,j}^k}{2\Delta x}, \dfrac{\alpha_{1\,i,j+1}^k - \alpha_{1\,i,j-1}^k}{2\Delta y}\Big)$
     - Compute $\vec{n}_{i,j}^k = \dfrac{\nabla\alpha_{1\,i,j}^k}{|\alpha_{1\,i,j}^k|}$ at cell centers
   - Compute curvature at cell centers:

     $\kappa_{i,j}^k = -\nabla \cdot \vec{n}_{i,j}^k = -\Big(\dfrac{n_{x,i+1,j}^k - n_{x,i-1,j}^k}{2\Delta x} + \dfrac{n_{y,i,j+1}^k - n_{y,i,j-1}^k}{2\Delta y}\Big)$

- Compute the surface tension forces on the faces:

$$\mathcal{F}^k_{x,i-1/2,j} = \sigma \frac{\kappa^k_{i,j} + \kappa^k_{i-1,j}}{2} \frac{\alpha^k_{1\,i,j} - \alpha^k_{1\,i-1,j}}{\Delta x}$$

$$\mathcal{F}^k_{y,i,j-1/2} = \sigma \frac{\kappa^k_{i,j} + \kappa^k_{i,j-1}}{2} \frac{\alpha^k_{1\,i,j} - \alpha^k_{1\,i,j-1}}{\Delta y}$$

4. Compute the mass transfer term at time-step k at the cell centers:
   - Compute the saturation pressure $p^k_{\text{sat}_{i,j}}$ using $T^k_{i,j}$ and Antoine relation, then calculate the corresponding vapor saturation:

$$\xi_{sat}{}^k_{i,j} = \frac{p^k_{\text{sat}_{i,j}}}{p^k_{\text{sat}_{i,j}} + (p^k_0 - p^k_{\text{sat}_{i,j}}) \frac{M_a}{M_v}}$$

   - $\mathcal{M}^k_{i,j} = \alpha^k_{1\,i,j}(1 - \alpha^k_{1\,i,j}) \dfrac{(\rho_2\alpha_2)^k_{i,j}\,(\xi^k_{i,j} - \xi_{sat}{}^k_{i,j})}{\tau^k_\xi}$
5. Compute (α_1) & $(\alpha_2\rho_2)$ at time-step $k+1$:
   - Compute re-sharpening flux at cell centers: $\vec{F}^k_{i,j} = \alpha^k_{1\,i,j}(\alpha^k_{1\,i,j} - 1)\vec{n}^k_{i,j}$
   - Compute artificial fluxes on the faces of cells:

$$R^k_{x,i-1/2,j} = \Xi\Big(\frac{F^k_{x,i,j} + F^k_{x,i-1,j}}{2} + \varepsilon_I \frac{\alpha^k_{1\,i,j} - \alpha^k_{1\,i-1,j}}{\Delta x}\Big)$$

$$R^k_{y,i,j-1/2} = \Xi\Big(\frac{F^k_{y,i,j} + F^k_{y,i,j-1}}{2} + \varepsilon_I \frac{\alpha^k_{1\,i,j} - \alpha^k_{1\,i,j-1}}{\Delta y}\Big)$$

   - Update α_1 at the new time-step:

$$(\alpha_{1\,i,j})^{k+1} = \alpha^k_{1\,i,j} + (\Delta t^{k+1})\Big(\frac{-(u^k_{i+1/2,j}\alpha^k_{1\,i+1/2,j} - u^k_{i-1/2,j}\alpha^k_{1\,i-1/2,j}) + (R^k_{x,i+1/2,j} - R^k_{x,i-1/2,j})}{\Delta x} + \frac{-(v^k_{i,j+1/2}\alpha^k_{1\,i,j+1/2} - v^k_{i,j-1/2}\alpha^k_{1\,i,j-1/2}) + (R^k_{y,i,j+1/2} - R^k_{y,i,j-1/2})}{\Delta y} + \frac{\mathcal{M}^k_{i,j}}{\rho_1}\Big)$$

   - Computing $(\alpha_2\rho_2)^{k+1}_{i,j}$ using eq. (61b) is analogous.
6. Compute ξ at time-step $k+1$:
   - Compute diffusion fluxes on the faces of cells:

$$\mathbb{F}^k_{x,i-1/2,j} = (\alpha_2\rho_2)^k_{i-1/2,j}\, D_{va}\, \frac{\xi^k_{i,j} - \xi^k_{i-1,j}}{\Delta x}$$

$$\mathbb{F}^k_{y,i,j-1/2} = (\alpha_2\rho_2)^k_{i,j-1/2}\, D_{va}\, \frac{\xi^k_{i,j} - \xi^k_{i,j-1}}{\Delta y}$$

   - Update $(\alpha_2\rho_2\xi)$ at the time-step $k+1$:

$$\begin{aligned}(\alpha_2\rho_2\xi)^{k+1}_{i,j} = (\alpha_2\rho_2\xi)^k_{i,j} + (\Delta t^{k+1})\Bigg(&\frac{-(u^k_{i+1/2,j}(\alpha_2\rho_2\xi)^k_{i+1/2,j} - u^k_{i-1/2,j}(\alpha_2\rho_2\xi)^k_{i-1/2,j})}{\Delta x}\\ &+ \frac{(\mathbb{F}^k_{x,i+1/2,j} - \mathbb{F}^k_{x,i-1/2,j}) + ((\rho_2\xi)^k_{i+1/2,j}R^k_{x,i+1/2,j} - (\rho_2\xi)^k_{i-1/2,j}R^k_{x,i-1/2,j})}{\Delta x}\\ &+ \frac{-(v^k_{i,j+1/2}(\alpha_2\rho_2\xi)^k_{i,j+1/2} - v^k_{i,j-1/2}(\alpha_2\rho_2\xi)^k_{i,j-1/2})}{\Delta y}\\ &+ \frac{(\mathbb{F}^k_{y,i,j+1/2} - \mathbb{F}^k_{y,i,j-1/2}) + ((\rho_2\xi)^k_{i,j+1/2}R^k_{y,i,j+1/2} - (\rho_2\xi)^k_{i,j-1/2}R^k_{y,i,j-1/2})}{\Delta y} - \mathcal{M}^k_{i,j}\Bigg)\end{aligned}$$

   - Compute ξ at the new time-step: $\xi^{k+1}_{i,j} = (\alpha_2\rho_2\xi)^{k+1}_{i,j} / (\rho_2\alpha_2)^{k+1}_{i,j}$
7. Update the $(\rho\kappa_p)$ at the time-step $k+1$, using $(\alpha_2\rho_2)^{k+1}_{i,j}$, $(\alpha_1)^{k+1}_{i,j}$, $\xi^{k+1}_{i,j}$ and following steps 1 & 2.
8. Compute enthalpy & temperature at time-step $k+1$:
   - Calculate the enthalpy of each phase on the cell faces:

$$h^k_{1\,i-1/2,j} = \kappa_{p1}T^k_{i-1/2,j} + \eta_1;\; h^k_{2\,i-1/2,j} = \kappa^k_{p2\,i-1/2,j}\, T^k_{i-1/2,j} + \eta_2$$

   - Compute energy fluxes on the faces of cells:

$$(HU)^k_{i-1/2,j} = (\rho h)^k_{i-1/2,j}u^k_{i-1/2,j} - (\rho_1 h^k_{1\,i-1/2,j} - \rho_2{}^k_{i-1/2,j}\, h^k_{2\,i-1/2,j})R^k_{x,i-1/2,j}$$

$$(HV)^k_{i,j-1/2} = (\rho h)^k_{i,j-1/2}v^k_{i,j-1/2} - (\rho_1 h^k_{1\,i,j-1/2} - \rho_2{}^k_{i,j-1/2}\, h^k_{2\,i,j-1/2})R^k_{y,i,j-1/2}$$

   - Calculate heat diffusion fluxes on the faces of cells:

$$\mathcal{T}^k_{x,i-1/2,j} = \lambda^k_{i-1/2,j} \frac{T^k_{i,j} - T^k_{i-1,j}}{\Delta x}$$

$$\mathcal{T}^k_{y,i,j-1/2} = \lambda^k_{i,j-1/2}\frac{T^k_{i,j} - T^k_{i,j-1}}{\Delta y}$$

- Update (ρh) to the time-step $k+1$:

$$(\rho h)^{k+1}_{i,j} = (\rho h)^k_{i,j} + (\Delta t^{k+1})(\frac{-((HU)^k_{i+1/2,j} - (HU)^k_{i-1/2,j}) + (\mathcal{T}^k_{x,i+1/2,j} - \mathcal{T}^k_{x,i-1/2,j})}{\Delta x} + \frac{-((HV)^k_{i,j+1/2} - (HV)^k_{i,j-1/2}) + (\mathcal{T}^k_{y,i,j+1/2} - \mathcal{T}^k_{y,i,j-1/2})}{\Delta y})$$

- $T^{k+1}_{i,j} = \dfrac{(\rho h)^{k+1}_{i,j} - (\,\rho_1(\alpha_{1\,i,j})^{k+1}\eta_1 + (\alpha_2\rho_2)^{k+1}_{i,j}\eta_2\,)}{(\rho\kappa_p)^{k+1}_{i,j}}$

9. Update the thermodynamic pressure (p_0) at time-step $k+1$:

$$p^{k+1}_0 = \frac{\sum_{i=1}^{N_x}\sum_{j=1}^{N_y}(\rho_2\alpha_2)^{k+1}_{i,j}\Delta x\Delta y}{\sum_{i=1}^{N_x}\sum_{j=1}^{N_y}\frac{(1-\alpha_1{}^{k+1}_{i,j})M_2{}^{k+1}_{i,j}}{T^{k+1}_{i,j}\mathcal{R}}\Delta x\Delta y}$$

10. Update mixture density (ρ) at time-step $k+1$ using $\xi^{k+1}_{i,j}$, $T^{k+1}_{i,j}$, p^{k+1}_0 and following step 1 & 2.
11. Update the mass transfer term, $\mathcal{M}$, at time-step $k+1$ at the cell centers, similar to step 4.
12. Compute viscous stresses, $\tau^k_{xx,i,j}$, $\tau^k_{xy,i-1/2,j-1/2}$, $\tau^k_{yy,i,j}$ and $\tau^k_{yx,i-1/2,j-1/2}$ using $\mu^k_{i,j}$, $u^k_{i-1/2,j}$ and $v^k_{i,j-1/2}$ fields. Standard linear interpolation operators are used for calculating $\mu^k_{i-1/2,j-1/2}$ values.
13. Compute mass flux on the faces:

$$U^k_{i-1/2,j} = (\rho u)^k_{i-1/2,j} - (\rho_1 - \rho^k_{2\,i-1/2,j})R^k_{x,i-1/2,j}$$
$$V^k_{i,j-1/2} = (\rho v)^k_{i,j-1/2} - (\rho_1 - \rho^k_{2\,i,j-1/2})R^k_{y,i,j-1/2}$$

14. Compute the intermediate values for ρu and ρv:

$$(\rho u)^{**}_{i-1/2,j} = (\rho u)^k_{i-1/2,j} - (\Delta t^{k+1})((\frac{\frac{U^k_{i+1/2,j}+U^k_{i-1/2,j}}{2}\frac{u^k_{i+1/2,j}+u^k_{i-1/2,j}}{2} - \frac{U^k_{i-1/2,j}+U^k_{i-3/2,j}}{2}\frac{u^k_{i-1/2,j}+u^k_{i-3/2,j}}{2}}{\Delta x} + \frac{V^k_{i-1/2,j+1/2}\frac{u^k_{i-1/2,j+1}+u^k_{i-1/2,j}}{2} - V^k_{i-1/2,j-1/2}\frac{u^k_{i-1/2,j}+u^k_{i-1/2,j-1}}{2}}{\Delta y}) - \frac{\tau^k_{xx,i,j}-\tau^k_{xx,i-1,j}}{\Delta x} - \frac{\tau^k_{xy,i-1/2,j+1/2}-\tau^k_{xy,i-1/2,j-1/2}}{\Delta y} - \mathcal{F}^{k+1}_{x,i-1/2,j})$$

$$(\rho v)^{**}_{i,j-1/2} = (\rho v)^k_{i,j-1/2} - (\Delta t^{k+1})((\frac{U^k_{i+1/2,j-1/2}\frac{v^k_{i+1,j-1/2}+v^k_{i,j-1/2}}{2} - U^k_{i-1/2,j-1/2}\frac{v^k_{i,j-1/2}+v^k_{i-1,j-1/2}}{2}}{\Delta x} + \frac{\frac{V^k_{i,j+1/2}+V^k_{i,j-1/2}}{2}\frac{v^k_{i,j+1/2}+v^k_{i,j-1/2}}{2} - \frac{V^k_{i,j-1/2}+V^k_{i,j-3/2}}{2}\frac{v^k_{i,j-1/2}+v^k_{i,j-3/2}}{2}}{\Delta y}) - \frac{\tau^k_{yy,i,j}-\tau^k_{yy,i,j-1}}{\Delta y} - \frac{\tau^k_{yx,i+1/2,j-1/2}-\tau^k_{yx,i-1/2,j-1/2}}{\Delta x} - \mathcal{F}^{k+1}_{y,i,j-1/2})$$

15. Compute intermediate value of velocity (momentum per unit mass):

$$u^{**}_{i-1/2,j} = \frac{(\rho u)^{**}_{i-1/2,j}}{\rho^{k+1}_{i-1/2,j}}$$
$$v^{**}_{i,j-1/2} = \frac{(\rho v)^{**}_{i,j-1/2}}{\rho^{k+1}_{i,j-1/2}}$$

16. Update the intermediate velocity with the contribution from terms due to the time-pressure splitting, as in [10], [111]:

$$u^{*}_{i-1/2,j} = u^{**}_{i-1/2,j} - \frac{\Delta t^{k+1}}{\rho_0}((1-\frac{\rho_0}{\rho^{k+1}}\frac{\hat{p}_{i,j}-\hat{p}_{i-1,j}}{\Delta x}) + \frac{p^k_{i,j}-p^k_{i-1,j}}{\Delta x})$$
$$v^{*}_{i,j-1/2} = v^{**}_{i,j-1/2} - \frac{\Delta t^{k+1}}{\rho_0}((1-\frac{\rho_0}{\rho^{k+1}}\frac{\hat{p}_{i,j}-\hat{p}_{i,j-1}}{\Delta y}) + \frac{p^k_{i,j}-p^k_{i,j-1}}{\Delta y})$$

Here, ρ_0 is the minimum value of the density field in the computational domain and $\hat{p}$ represents the time-extrapolated pressure between the current and the older time step, i.e. $\hat{p} = (1 + \Delta t^{k+1}/\Delta t^k)p^k - (\Delta t^{k+1}/\Delta t^k)p^{k-1}$.

17. Compute the pressure correction that would enforce the velocity divergence field:
    - Calculate the velocity divergence field at the cell center and at the time-step $k+1$:
      - Calculate the mixture quantities, $\bar{Z}, \bar{B}, \bar{D}, \bar{K}_S$, using eqs. (38a), (38b), (38c), (38d) and the updated properties at the cell centers and at the time-step $k+1$.
      - Calculate the fluxes $\mathcal{T}$ and $\mathbb{F}$ at time step $k+1$ similar to the steps 5 and 6.
      - Compute the thermodynamic pressure variation, (dp_0/dt) at time-step $k+1$ using eq. (42) and the previous updated properties.
      - $$(\vec{\nabla}\cdot\vec{u})^{k+1}_{i,j} = \bar{Z}^{k+1}_{i,j}\mathcal{M}^{k+1}_{i,j} + \bar{B}^{k+1}_{i,j}\left(\frac{\mathcal{T}^{k+1}_{x,i+1/2,j} - \mathcal{T}^{k+1}_{x,i-1/2,j}}{\Delta x} + \frac{\mathcal{T}^{k+1}_{y,i,j+1/2} - \mathcal{T}^{k+1}_{y,i,j-1/2}}{\Delta y}\right) + \bar{D}^{k+1}_{i,j}\left(\frac{\mathbb{F}^{k+1}_{x,i+1/2,j} - \mathbb{F}^{k+1}_{x,i-1/2,j}}{\Delta x} + \frac{\mathbb{F}^{k+1}_{y,i,j+1/2} - \mathbb{F}^{k+1}_{y,i,j-1/2}}{\Delta y}\right) - \bar{K}^{k+1}_{S,i,j}\left(\frac{dp_0}{dt}\right)^{k+1}$$
    - Compute RHS of Poisson system at the cell center which is equivalent to:
      $$(RHS)^k_{i,j} = \frac{\rho_0}{\Delta t^{k+1}}\left(\frac{{u^*}_{i+1/2,j} - {u^*}_{i-1/2,j}}{\Delta x} + \frac{{v^*}_{i,j+1/2} - {v^*}_{i,j-1/2}}{\Delta y} - (\vec{\nabla}\cdot\vec{u})^{k+1}_{i,j}\right)$$
    - Solve the constant coefficient Poisson equation with the method of eigenexpansion technique, to find $\psi_{i,j} = p^{k+1}_{i,j} - p^k_{i,j}$:
      $$\frac{\frac{\psi_{i+1,j}-\psi_{i,j}}{\Delta x} - \frac{\psi_{i,j}-\psi_{i-1,j}}{\Delta x}}{\Delta x} + \frac{\frac{\psi_{i,j+1}-\psi_{i,j}}{\Delta y} - \frac{\psi_{i,j}-\psi_{i,j-1}}{\Delta y}}{\Delta y} = (RHS)^k_{i,j}$$
18. The corrector step:
    - Correct the velocity field in order to impose divergence constrain at time step $k+1$:
      $$u^{k+1}_{i-1/2,j} = u^k_{i-1/2,j} - \frac{\Delta t^{k+1}}{\rho_0}\left(\frac{\psi_{i,j}-\psi_{i-1,j}}{\Delta x}\right)$$
      $$v^{k+1}_{i,j-1/2} = v^k_{i,j-1/2} - \frac{\Delta t^{k+1}}{\rho_0}\left(\frac{\psi_{i,j}-\psi_{i,j-1}}{\Delta y}\right)$$
    - Update the pressure value at time-step $k+1$:
      $$p^{k+1}_{i,j} = p^k_{i,j} + \psi_{i,j}$$
19. Advance time $t = t + \Delta t$, return to step 1 with $k = k+1$

Data availability

Data will be made available on request.

References

[1] R.A. Shaw, Particle-turbulence interactions in atmospheric clouds, Annu. Rev. Fluid Mech. (ISSN 1545-4479) 35 (2003) 183–227, https://doi.org/10.1146/annurev.fluid.35.101101.161125, https://www.annualreviews.org/content/journals/10.1146/annurev.fluid.35.101101.161125.

[2] W.K. Melville, The role of surface-wave breaking in air-sea interaction, Annu. Rev. Fluid Mech. (ISSN 1545-4479) 28 (1996) 279–321, https://doi.org/10.1146/annurev.fl.28.010196.001431, https://www.annualreviews.org/content/journals/10.1146/annurev.fl.28.010196.001431.

[3] W.A. Sirignano, Fluid Dynamics and Transport of Droplets and Sprays, Cambridge University Press, 1999.

[4] Y. Sato, M. Sadatomi, K. Sekoguchi, Momentum and heat transfer in two-phase bubble flow—I. Theory, Int. J. Multiph. Flow (ISSN 0301-9322) 7 (2) (1981) 167–177, https://doi.org/10.1016/0301-9322(81)90003-3, https://www.sciencedirect.com/science/article/pii/0301932281900033.

[5] R. Clift, J. Grace, M. Weber, Bubbles, Drops, and Particles, Courier Corporation, 01 1978.

[6] B. Abramzon, W.A. Sirignano, Droplet vaporization model for spray combustion calculations, Int. J. Heat Mass Transf. (ISSN 0017-9310) 32 (9) (1989) 1605–1618, https://doi.org/10.1016/0017-9310(89)90043-4, https://www.sciencedirect.com/science/article/pii/0017931089900434.

[7] C.K. Law, Recent advances in droplet vaporization and combustion, Prog. Energy Combust. Sci. (ISSN 0360-1285) 8 (3) (1982) 171–201, https://doi.org/10.1016/0360-1285(82)90011-9, https://www.sciencedirect.com/science/article/pii/0360128582900119.

[8] A. Cuoci, M. Mehl, G. Buzzi-Ferraris, T. Faravelli, D. Manca, E. Ranzi, Autoignition and burning rates of fuel droplets under microgravity, Combust. Flame (ISSN 0010-2180) 143 (3) (2005) 211–226, https://doi.org/10.1016/j.combustflame.2005.06.003, https://www.sciencedirect.com/science/article/pii/S0010218005001525.

[9] A. Prosperetti, G. Tryggvason, Computational Methods for Multiphase Flow, Cambridge University Press, 2007.

[10] S.O. Unverdi, G. Tryggvason, A front-tracking method for viscous, incompressible, multi-fluid flows, J. Comput. Phys. (ISSN 0021-9991) 100 (1) (1992) 25–37, https://doi.org/10.1016/0021-9991(92)90307-K, https://www.sciencedirect.com/science/article/pii/002199919290307K.

[11] T.V. Vu, G. Tryggvason, S. Homma, John C. Wells, Numerical investigations of drop solidification on a cold plate in the presence of volume change, Int. J. Multiph. Flow 76 (2015) 73–85, https://doi.org/10.1016/j.ijmultiphaseflow.2015.07.005, https://www.scopus.com/inward/record.uri?eid=2-s2.0-84938150805&doi=10.1016%2fj.ijmultiphaseflow.2015.07.005&partnerID=40&md5=d7c28c48ade17f8d7fa63917bfa878cf, Cited by: 88.

[12] D. Juric, G. Tryggvason, Computations of boiling flows, Int. J. Multiph. Flow (ISSN 0301-9322) 24 (3) (1998) 387–410, https://doi.org/10.1016/S0301-9322(97)00050-5, https://www.sciencedirect.com/science/article/pii/S0301932297000505.

[13] M. Irfan, M. Muradoglu, A front tracking method for direct numerical simulation of evaporation process in a multiphase system, J. Comput. Phys. (ISSN 0021-9991) 337 (2017) 132–153, https://doi.org/10.1016/j.jcp.2017.02.036, https://www.sciencedirect.com/science/article/pii/S0021999117301304.

[14] J. Lu, G. Tryggvason, Direct numerical simulations of multifluid flows in a vertical channel undergoing topology changes, Phys. Rev. Fluids 3 (8) (2018), https://doi.org/10.1103/PhysRevFluids.3.084401, https://www.scopus.com/inward/record.uri?eid=2-s2.0-85052917166&doi=10.1103%2fPhysRevFluids.3.084401&partnerID=40&md5=0fb0cc1539150d39b1e072364e27ce83, Cited by: 30; All Open Access, Bronze Open Access.

[15] M.N. Farooqi, D. Izbassarov, M. Muradoğlu, D. Unat, Communication analysis and optimization of 3D front tracking method for multiphase flow simulations, Int. J. High Perform. Comput. Appl. 33 (1) (2019) 67–80, https://doi.org/10.1177/1094342017694426.

[16] C.W. Hirt, B.D. Nichols, Volume of fluid (vof) method for the dynamics of free boundaries, J. Comput. Phys. 39 (1) (1981) 201–225, https://doi.org/10.1016/0021-9991(81)90145-5, https://www.scopus.com/inward/record.uri?eid=2-s2.0-0019367877&doi=10.1016%2f0021-9991%2881%2990145-5&partnerID=40&md5=8233ceed366c24956ec15cbb5abcf451, Cited by: 13779.

[17] J.A. Sethian, P. Smereka, Level set methods for fluid interfaces, Annu. Rev. Fluid Mech. 35 (2003) 341–372, https://doi.org/10.1146/annurev.fluid.35.101101.161105, https://www.scopus.com/inward/record.uri?eid=2-s2.0-0242276905&doi=10.1146%2fannurev.fluid.35.101101.161105&partnerID=40&md5=db6c442e028ec648b799e639e22bafb1, Cited by: 812.

[18] M. Sussman, P. Smereka, S. Osher, A level set approach for computing solutions to incompressible two-phase flow, J. Comput. Phys. (ISSN 0021-9991) 114 (1) (1994) 146–159, https://doi.org/10.1006/jcph.1994.1155, https://www.sciencedirect.com/science/article/pii/S0021999184711557.

[19] R.S. Qin, H.K. Bhadeshia, Phase field method, Mater. Sci. Technol. 26 (7) (2010) 803–811, https://doi.org/10.1179/174328409X453190, https://www.scopus.com/inward/record.uri?eid=2-s2.0-77955318688&doi=10.1179%2f174328409X453190&partnerID=40&md5=4ff1ba3d344885455bccd10bd98192dc, Cited by: 146.

[20] L.-Q. Chen, Phase-field models for microstructure evolution, Annu. Rev. Mater. Sci. 32 (2002) 113–140, https://doi.org/10.1146/annurev.matsci.32.112001.132041, https://www.scopus.com/inward/record.uri?eid=2-s2.0-0036036465&doi=10.1146%2fannurev.matsci.32.112001.132041&partnerID=40&md5=e15fcf010d600fb147674ce3a226aa5e, Cited by: 2392.

[21] S. Hardt, F. Wondra, Evaporation model for interfacial flows based on a continuum-field representation of the source terms, J. Comput. Phys. (ISSN 0021-9991) 227 (11) (2008) 5871–5895, https://doi.org/10.1016/j.jcp.2008.02.020, https://www.sciencedirect.com/science/article/pii/S0021999108001228.

[22] C. Kunkelmann, P. Stephan, CFD simulation of boiling flows using the volume-of-fluid method within OpenFOAM, Numer. Heat Transf., Part A, Appl. 56 (8) (2009) 631–646, https://doi.org/10.1080/10407780903423908.

[23] J. Schlottke, B. Weigand, Direct numerical simulation of evaporating droplets, J. Comput. Phys. (ISSN 0021-9991) 227 (10) (2008) 5215–5237, https://doi.org/10.1016/j.jcp.2008.01.042, https://www.sciencedirect.com/science/article/pii/S0021999108000740.

[24] Y. Sato, B. Ničeno, A sharp-interface phase change model for a mass-conservative interface tracking method, J. Comput. Phys. (ISSN 0021-9991) 249 (2013) 127–161, https://doi.org/10.1016/j.jcp.2013.04.035, https://www.sciencedirect.com/science/article/pii/S0021999113003197.

[25] N. Scapin, P. Costa, L. Brandt, A volume-of-fluid method for interface-resolved simulations of phase-changing two-fluid flows, J. Comput. Phys. 407 (2020) 109251.

[26] L.C. Malan, A.G. Malan, S. Zaleski, P.G. Rousseau, A geometric vof method for interface resolved phase change and conservative thermal energy advection, J. Comput. Phys. (ISSN 0021-9991) 426 (2021) 109920, https://doi.org/10.1016/j.jcp.2020.109920, https://www.sciencedirect.com/science/article/pii/S002199912030694X.

[27] J. Palmore, O. Desjardins, A volume of fluid framework for interface-resolved simulations of vaporizing liquid-gas flows, J. Comput. Phys. (ISSN 0021-9991) 399 (2019) 108954, https://doi.org/10.1016/j.jcp.2019.108954, https://www.sciencedirect.com/science/article/pii/S002199911930659X.

[28] S. Zhao, J. Zhang, M.-J. Ni, Boiling and evaporation model for liquid-gas flows: a sharp and conservative method based on the geometrical vof approach, J. Comput. Phys. (ISSN 0021-9991) 452 (2022) 110908, https://doi.org/10.1016/j.jcp.2021.110908, https://www.sciencedirect.com/science/article/pii/S0021999121008032.

[29] E. Cipriano, A. Essamade Saufi, A. Frassoldati, T. Faravelli, S. Popinet, A. Cuoci, Multicomponent droplet evaporation in a geometric volume-of-fluid framework, J. Comput. Phys. (ISSN 0021-9991) 507 (2024) 112955, https://doi.org/10.1016/j.jcp.2024.112955, https://www.sciencedirect.com/science/article/pii/S0021999124002043.

[30] S. Zamani Salimi, N. Scapin, E.-R. Popescu, P. Costa, L. Brandt, A volume-of-fluid method for multicomponent droplet evaporation with Robin boundary conditions, J. Comput. Phys. (ISSN 0021-9991) (2024) 113211, https://doi.org/10.1016/j.jcp.2024.113211, https://www.sciencedirect.com/science/article/pii/S0021999124004601.

[31] G. Son, V.K. Dhir, Numerical simulation of film boiling near critical pressures with a level set method, J. Heat Transf. (ISSN 0022-1481) 120 (1) (02 1998) 183–192, https://doi.org/10.1115/1.2830042.

[32] S. Tanguy, T. Ménard, A. Berlemont, A level set method for vaporizing two-phase flows, J. Comput. Phys. (ISSN 0021-9991) 221 (2) (2007) 837–853, https://doi.org/10.1016/j.jcp.2006.07.003, https://www.sciencedirect.com/science/article/pii/S0021999106003214.

[33] S. Tanguy, M. Sagan, B. Lalanne, F. Couderc, C. Colin, Benchmarks and numerical methods for the simulation of boiling flows, J. Comput. Phys. (ISSN 0021-9991) 264 (2014) 1–22, https://doi.org/10.1016/j.jcp.2014.01.014, https://www.sciencedirect.com/science/article/pii/S0021999114000412.

[34] L. Rueda Villegas, R. Alis, M. Lepilliez, S. Tanguy, A ghost fluid/level set method for boiling flows and liquid evaporation: application to the leidenfrost effect, J. Comput. Phys. (ISSN 0021-9991) 316 (2016) 789–813, https://doi.org/10.1016/j.jcp.2016.04.031, https://www.sciencedirect.com/science/article/pii/S0021999116300778.

[35] K. Luo, C. Shao, M. Chai, J. Fan, Level set method for atomization and evaporation simulations, Prog. Energy Combust. Sci. (ISSN 0360-1285) 73 (2019) 65–94, https://doi.org/10.1016/j.pecs.2019.03.001, https://www.sciencedirect.com/science/article/pii/S0360128518301710.

[36] Q. Zhang, T.-Z. Qian, X.-P. Wang, Phase field simulation of a droplet impacting a solid surface, Phys. Fluids (ISSN 1070-6631) 28 (2) (2016) 022103, https://doi.org/10.1063/1.4940995.

[37] H. Yu, X. Yang, Numerical approximations for a phase-field moving contact line model with variable densities and viscosities, J. Comput. Phys. (ISSN 0021-9991) 334 (2017) 665–686, https://doi.org/10.1016/j.jcp.2017.01.026, https://www.sciencedirect.com/science/article/pii/S0021999117300426.

[38] D. Jacqmin, Calculation of two-phase Navier–Stokes flows using phase-field modeling, J. Comput. Phys. (ISSN 0021-9991) 155 (1) (1999) 96–127, https://doi.org/10.1006/jcph.1999.6332, https://www.sciencedirect.com/science/article/pii/S0021999199963325.

[39] J. Shen, X. Yang, A phase-field model and its numerical approximation for two-phase incompressible flows with different densities and viscosities, SIAM J. Sci. Comput. 32 (3) (2010) 1159–1179, https://doi.org/10.1137/09075860X.

[40] Z. Huang, G. Lin, A.M. Ardekani, Consistent, essentially conservative and balanced-force phase-field method to model incompressible two-phase flows, J. Comput. Phys. 406 (2020), https://doi.org/10.1016/j.jcp.2019.109192, https://www.scopus.com/inward/record.uri?eid=2-s2.0-85078607074&doi=10.1016%2fj.jcp.2019.109192&partnerID=40&md5=cf9c5be36ec39652fce0cfe6e6188c26, Cited by: 33; All Open Access, Hybrid Gold Open Access.

[41] W. Zhang, A. Shahmardi, K.-S. Choi, O. Tammisola, L. Brandt, X. Mao, A phase-field method for three-phase flows with icing, J. Comput. Phys. (ISSN 0021-9991) 458 (2022) 111104, https://doi.org/10.1016/j.jcp.2022.111104, https://www.sciencedirect.com/science/article/pii/S0021999122001668.

[42] L. Brown, S. Jain, P. Moin, A phase field model for simulating the freezing of supercooled liquid droplets, Adv. Curr. Pract. Mobil. (ISSN 2641-9637) (Jun 2023), https://doi.org/10.4271/2023-01-1454.

[43] R. Jafari, T. Okutucu-Özyurt, Numerical simulation of flow boiling from an artificial cavity in a microchannel, Int. J. Heat Mass Transf. (ISSN 0017-9310) 97 (2016) 270–278, https://doi.org/10.1016/j.ijheatmasstransfer.2016.02.028, https://www.sciencedirect.com/science/article/pii/S0017931015304798.

[44] Z. Wang, X. Zheng, C. Chryssostomidis, G.E. Karniadakis, A phase-field method for boiling heat transfer, J. Comput. Phys. (ISSN 0021-9991) 435 (2021) 110239, https://doi.org/10.1016/j.jcp.2021.110239, https://www.sciencedirect.com/science/article/pii/S0021999121001340.

[45] P.J. Sáenz, K. Sefiane, J. Kim, O.K. Matar, P. Valluri, Evaporation of sessile drops: a three-dimensional approach, J. Fluid Mech. 772 (2015) 705–739.

[46] P. Yue, C. Zhou, J.J. Feng, Spontaneous shrinkage of drops and mass conservation in phase-field simulations, J. Comput. Phys. (ISSN 0021-9991) 223 (1) (2007) 1–9, https://doi.org/10.1016/j.jcp.2006.11.020, https://www.sciencedirect.com/science/article/pii/S0021999106005857.

[47] S. Dong, J. Shen, A time-stepping scheme involving constant coefficient matrices for phase-field simulations of two-phase incompressible flows with large density ratios, J. Comput. Phys. (ISSN 0021-9991) 231 (17) (2012) 5788–5804, https://doi.org/10.1016/j.jcp.2012.04.041, https://www.sciencedirect.com/science/article/pii/S0021999112002239.

[48] Y. Wang, C. Shu, J.Y. Shao, J. Wu, X.D. Niu, A mass-conserved diffuse interface method and its application for incompressible multiphase flows with large density ratio, J. Comput. Phys. (ISSN 0021-9991) 290 (2015) 336–351, https://doi.org/10.1016/j.jcp.2015.03.005, https://www.sciencedirect.com/science/article/pii/S0021999115001382.

[49] Y. Li, J.-I. Choi, J. Kim, A phase-field fluid modeling and computation with interfacial profile correction term, Commun. Nonlinear Sci. Numer. Simul. (ISSN 1007-5704) 30 (1) (2016) 84–100, https://doi.org/10.1016/j.cnsns.2015.06.012, https://www.sciencedirect.com/science/article/pii/S1007570415002130.

[50] Y. Sun, C. Beckermann, Sharp interface tracking using the phase-field equation, J. Comput. Phys. (ISSN 0021-9991) 220 (2) (2007) 626–653, https://doi.org/10.1016/j.jcp.2006.05.025, https://www.sciencedirect.com/science/article/pii/S0021999106002531.

[51] P.-H. Chiu, Y.-T. Lin, A conservative phase field method for solving incompressible two-phase flows, J. Comput. Phys. (ISSN 0021-9991) 230 (1) (2011) 185–204, https://doi.org/10.1016/j.jcp.2010.09.021, https://www.sciencedirect.com/science/article/pii/S0021999110005243.

[52] S. Mirjalili, C.B. Ivey, A. Mani, A conservative diffuse interface method for two-phase flows with provable boundedness properties, J. Comput. Phys. (ISSN 0021-9991) 401 (2020) 109006, https://doi.org/10.1016/j.jcp.2019.109006, https://www.sciencedirect.com/science/article/pii/S0021999119307119.

[53] E. Olsson, G. Kreiss, A conservative level set method for two phase flow, J. Comput. Phys. (ISSN 0021-9991) 210 (1) (2005) 225–246, https://doi.org/10.1016/j.jcp.2005.04.007, https://www.sciencedirect.com/science/article/pii/S0021999105002184.

[54] S.S. Jain, A. Mani, P. Moin, A conservative diffuse-interface method for compressible two-phase flows, J. Comput. Phys. 418 (109606) (2020).

[55] J.P. Van Doormaal, G.D. Raithby, B.H. McDonald, The segregated approach to predicting viscous compressible fluid flows, J. Turbomach. (ISSN 0889-504X) 109 (2) (1987) 268–277, https://doi.org/10.1115/1.3262097.

[56] M. Gallo, F. Magaletti, D. Cocco, C.M. Casciola, Nucleation and growth dynamics of vapour bubbles, J. Fluid Mech. 883 (2020) A14, https://doi.org/10.1017/jfm.2019.844.

[57] M.R. Baer, J.W. Nunziato, A two-phase mixture theory for the deflagration-to-detonation transition (DDT) in reactive granular materials, Int. J. Multiph. Flow 12 (1986) 861–889.

[58] R. Saurel, R. Abgrall, A multiphase Godunov method for compressible multifluid and multiphase flows, J. Comput. Phys. 150 (1999) 425–467.

[59] T. Flåtten, H. Lund, Relaxation two-phase models and the subcharacteristic condition, Math. Models Methods Appl. Sci. 21 (2011) 2379–2407.

[60] G. Linga, T. Flåtten, A hierarchy of non-equilibrium two-phase flow models, ESAIM Proc. Surv. 66 (2019) 109–143.

[61] R. Saurel, F. Petitpas, R.A. Berry, Simple and efficient relaxation methods for interfaces separating compressible fluids, cavitating flows and shocks in multiphase mixtures, J. Comput. Phys. 228 (2009) 1678–1712.

[62] G.-S. Yeom, K.-S. Chang, A modified HLLC-type Riemann solver for the compressible six-equation two-fluid model, Comput. Fluids (ISSN 0045-7930) 76 (2013) 86–104, https://doi.org/10.1016/j.compfluid.2013.01.021, https://www.sciencedirect.com/science/article/pii/S0045793013000455.

[63] M. Pelanti, K.-M. Shyue, A mixture-energy-consistent six-equation two-phase numerical model for fluids with interfaces, cavitation and evaporation waves, J. Comput. Phys. 259 (2014) 331–357.

[64] A.K. Kapila, R. Menikoff, J.B. Bdzil, S.F. Son, D.S. Stewart, Two-phase modeling of deflagration-to-detonation transition in granular materials: reduced equations, Phys. Fluids 13 (2001) 3002–3024.

[65] G. Allaire, S. Clerc, S. Kokh, A five-equation model for the simulation of interfaces between compressible fluids, J. Comput. Phys. 181 (2002) 577–616.

[66] A. Murrone, H. Guillard, A five-equation reduced model for compressible two-phase flows problems, J. Comput. Phys. 202 (2005) 664–698.

[67] G. Perigaud, R. Saurel, A compressible flow model with capillary effects, J. Comput. Phys. (ISSN 0021-9991) 209 (1) (2005) 139–178, https://doi.org/10.1016/j.jcp.2005.03.018, https://www.sciencedirect.com/science/article/pii/S0021999105001853.

[68] R.K. Shukla, C. Pantano, J.B. Freund, An interface capturing method for the simulation of multi-phase compressible flows, J. Comput. Phys. (ISSN 0021-9991) 229 (19) (2010) 7411–7439, https://doi.org/10.1016/j.jcp.2010.06.025, https://www.sciencedirect.com/science/article/pii/S0021999110003402.

[69] R. Abgrall, How to prevent pressure oscillations in multicomponent flow calculations: a quasi conservative approach, J. Comput. Phys. 125 (1996) 150–160.

[70] R. Saurel, R. Abgrall, A simple method for compressible multifluid flow, SIAM J. Sci. Comput. 71 (1999) 1115–1145.

[71] E. Johnsen, F. Ham, Preventing numerical errors generated by interface-capturing schemes in compressible multi-material flows, J. Comput. Phys. (ISSN 0021-9991) 231 (17) (2012) 5705–5717, https://doi.org/10.1016/j.jcp.2012.04.048, https://www.sciencedirect.com/science/article/pii/S0021999112002525.

[72] H. Lund, P. Aursand, Two-phase flow of CO_2 with phase transfer, Energy Proc. 23 (2012) 246–255.

[73] S. Le Martelot, R. Saurel, B. Nkonga, Towards the direct numerical simulation of nucleate boiling, Int. J. Multiph. Flow 66 (2014) 62–78.

[74] R. Saurel, P. Boivin, O. LeMétayer, A general formulation for cavitating, boiling and evaporating flows, Comput. Fluids 128 (2016) 53–64.

[75] A.D. Demou, N. Scapin, M. Pelanti, L. Brandt, A pressure-based diffuse interface method for low-Mach multiphase flows with mass transfer, J. Comput. Phys. 448 (110730) (2022).

[76] B. Re, R. Abgrall, A pressure-based method for weakly compressible two-phase flows under a Baer–Nunziato type model with generic equations of state and pressure and velocity disequilibrium, Int. J. Numer. Methods Fluids 94 (8) (2022) 1183–1232, https://doi.org/10.1002/fld.5087, https://onlinelibrary.wiley.com/doi/abs/10.1002/fld.5087.

[77] B. Re, R. Abgrall, Non-equilibrium model for weakly compressible multi-component flows: the hyperbolic operator, in: F. di Mare, A. Spinelli, M. Pini (Eds.), Non-Ideal Compressible Fluid Dynamics for Propulsion and Power. NICFD 2018, in: Lecture Notes in Mechanical Engineering., Springer, 2020.

[78] M.B. Kuhn, O. Desjardins, An all-Mach, low-dissipation strategy for simulating multiphase flows, J. Comput. Phys. (ISSN 0021-9991) 445 (2021) 110602, https://doi.org/10.1016/j.jcp.2021.110602, https://www.sciencedirect.com/science/article/pii/S0021999121004976.

[79] F. Denner, C.-N. Xiao, B.G.M. van Wachem, Pressure-based algorithm for compressible interfacial flows with acoustically-conservative interface discretisation, J. Comput. Phys. (ISSN 0021-9991) 367 (2018) 192–234, https://doi.org/10.1016/j.jcp.2018.04.028, https://www.sciencedirect.com/science/article/pii/S0021999118302535.

[80] D. Fuster, S. Popinet, An all-Mach method for the simulation of bubble dynamics problems in the presence of surface tension, J. Comput. Phys. (ISSN 0021-9991) 374 (2018) 752–768, https://doi.org/10.1016/j.jcp.2018.07.055, https://www.sciencedirect.com/science/article/pii/S0021999118305187.

[81] M. Jemison, M. Sussman, M. Arienti, Compressible, multiphase semi-implicit method with moment of fluid interface representation, J. Comput. Phys. (ISSN 0021-9991) 279 (2014) 182–217, https://doi.org/10.1016/j.jcp.2014.09.005, https://www.sciencedirect.com/science/article/pii/S0021999114006317.

[82] N. Scapin, F. Dalla Barba, G. Lupo, Rosti M. E, C. Duwig, L. Brandt, Finite-size evaporating droplets in weakly compressible homogeneous shear turbulence, J. Fluid Mech. 934 (2022) A15, https://doi.org/10.1017/jfm.2021.1140.

[83] E.A. Wenzel, M. Arienti, A conservative, interface-resolved, compressible framework for the modeling and simulation of liquid/gas phase change, J. Comput. Phys. (ISSN 0021-9991) 477 (2023) 111957, https://doi.org/10.1016/j.jcp.2023.111957, https://www.sciencedirect.com/science/article/pii/S0021999123000529.

[84] S. Mirjalili, C.B. Ivey, A. Mani, Comparison between the diffuse interface and volume of fluid methods for simulating two-phase flows, Int. J. Multiph. Flow (ISSN 0301-9322) 116 (2019) 221–238, https://doi.org/10.1016/j.ijmultiphaseflow.2019.04.019, https://www.sciencedirect.com/science/article/pii/S0301932218309030.

[85] N. Scapin, A. Shahmardi, W.H.R. Chan, S.S. Jain, S. Mirjalili, M. Pelanti, L. Brandt, A mass-conserving pressure-based method for two-phase flows with phase change, in: Proceedings of the Summer Program 2022, Stanford University Center for Turbulence Research, 2022.

[86] A. Chiapolino, P. Boivin, R. Saurel, A simple and fast phase transition relaxation solver for compressible multicomponent two-phase flows, Comput. Fluids 150 (2017) 31–45.
[87] M. Pelanti, K.-M. Shyue, A numerical model for multiphase liquid-vapor-gas flows with interfaces and cavitation, Int. J. Multiph. Flow 113 (2019) 208–230.
[88] S. Klainerman, A. Majda, Compressible and incompressible fluids, Commun. Pure Appl. Math. 35 (1982) 629–651.
[89] S. Klainerman, A. Majda, Singular limits of quasilinear hyperbolic systems with large parameters and the incompressible limit of compressible fluids, Commun. Pure Appl. Math. 34 (1981) 481–524.
[90] A. Majda, J. Sethian, The derivation and numerical solution of the equations for zero Mach number combustion, Combust. Sci. Technol. 42 (1985) 185–205.
[91] S. Schochet, Fast singular limits of hyperbolic PDEs, J. Differ. Equ. 114 (1994) 476–512.
[92] G. Metivier, S. Schochet, The incompressible limit of the non-isentropic Euler equations, Arch. Ration. Mech. Anal. 158 (1) (2001) 61–90.
[93] T. Alazard, Low Mach number limit of the full Navier–Stokes equations, Arch. Ration. Mech. Anal. 180 (1) (2006) 173.
[94] M. Duarte, A.S. Almgren, J.B. Bell, A low Mach number model for moist atmospheric flows, J. Atmos. Sci. 72 (4) (2015) 1605–1620.
[95] R. Saurel, F. Petitpas, R. Abgrall, Modelling phase transition in metastable liquids: application to cavitating and flashing flows, J. Fluid Mech. 607 (2008) 313–350.
[96] A. Zein, M. Hantke, G. Warnecke, Modeling phase transition for compressible two-phase flows applied to metastable liquids, J. Comput. Phys. 229 (2010) 2964–2998.
[97] M. De Lorenzo, P. Lafon, M. Pelanti, A hyperbolic phase-transition model with non-instantaneous EoS-independent relaxation procedures, J. Comput. Phys. 379 (2019) 279–308.
[98] M. Pelanti, Arbitrary-rate relaxation techniques for the numerical modeling of compressible two-phase flows with heat and mass transfer, Int. J. Multiph. Flow 153 (2022) 104097.
[99] I. Müller, W.H. Müller, Fundamentals of Thermodynamics and Applications, Springer, 2009.
[100] S.S. Jain, Accurate conservative phase-field method for simulation of two-phase flows, J. Comput. Phys. 469 (11152) (2022).
[101] S. Mirjalili, M. Khanwale, A. Mani, Consistent modeling of scalar transport in multiphase flows using conservative phase field methods, in: Proceedings of the Summer Program 2022, Stanford University Center for Turbulence Research, 2022.
[102] S. Patankar, Numerical Heat Transfer and Fluid Flow, 1 edition, CRC Press, 1980.
[103] A.J. Chorin, Numerical solution of the Navier-Stokes equations, Math. Comput. 22 (104) (1968) 745–762, https://doi.org/10.1090/S0025-5718-1968-0242392-2.
[104] M.S. Dodd, A. Ferrante, A fast pressure-correction method for incompressible two-fluid flows, J. Comput. Phys. (ISSN 0021-9991) 273 (2014) 416–434, https://doi.org/10.1016/j.jcp.2014.05.024, https://www.sciencedirect.com/science/article/pii/S0021999114003702.
[105] P. Moin, R. Verzicco, On the suitability of second-order accurate discretizations for turbulent flow simulations, Eur. J. Mech. B, Fluids (ISSN 0997-7546) 55 (2016) 242–245, https://doi.org/10.1016/j.euromechflu.2015.10.006, https://www.sciencedirect.com/science/article/pii/S0997754615302582, Vortical Structures and Wall Turbulence.
[106] S.S. Jain, A. Mani, A computational model for transport of immiscible scalars in two-phase flows, J. Comput. Phys. (ISSN 0021-9991) 476 (2023) 111843, https://doi.org/10.1016/j.jcp.2022.111843, https://www.sciencedirect.com/science/article/pii/S0021999122009068.
[107] S. Mirjalili, A. Mani, Consistent, energy-conserving momentum transport for simulations of two-phase flows using the phase field equations, J. Comput. Phys. (ISSN 0021-9991) 426 (2021) 109918, https://doi.org/10.1016/j.jcp.2020.109918, https://www.sciencedirect.com/science/article/pii/S0021999120306926.
[108] L. Fei, F. Qin, G. Wang, K.H. Luo, D. Derome, J. Carmeliet, Droplet evaporation in finite-size systems: theoretical analysis and mesoscopic modeling, Phys. Rev. E 105 (Feb 2022) 025101, https://doi.org/10.1103/PhysRevE.105.025101, https://link.aps.org/doi/10.1103/PhysRevE.105.025101.
[109] O. Le Métayer, R. Saurel, The Noble-Abel stiffened-gas equation of state, Phys. Fluids 28 (2016) 046102.
[110] F. Dalla Barba, N. Scapin, A.D. Demou, M.E. Rosti, F. Picano, L. Brandt, An interface capturing method for liquid-gas flows at low-Mach number, Comput. Fluids 216 (2021) 104789.
[111] M. Crialesi-Esposito, N. Scapin, A.D. Demou, M.E. Rosti, P. Costa, F. Spiga, L. Brandt, FluTAS: a GPU-accelerated finite difference code for multiphase flows, Comput. Phys. Commun. (ISSN 0010-4655) 284 (2023) 108602, https://doi.org/10.1016/j.cpc.2022.108602, https://www.sciencedirect.com/science/article/pii/S0010465522003216.